

1 **Application of Wave-current coupled Sediment Transport Models with**
2 **Variable Grain Properties for Coastal Morphodynamics: A Case Study of the**
3 **Changhua River, Hainan**

4 **Yuxi Wu^{1a}, Enjin Zhao^{1b,*}, Xiwen Li^{2c} and Shiyu Zhang^{2d}**

5 *1. College of Marine Science and Technology, China University of Geosciences, Wuhan 430074,*
6 *China.*

7 *2. Haikou Marine Geological Survey Center, China Geological Survey, Haikou 570100, China*

8 _____

9 * Corresponding author: Enjin Zhao (zhaoej@cug.edu.cn)

10 ^a Ms., Master of *China University of Geosciences, Wuhan*, Email: yuxiwu@cug.edu.cn

11 ^b Ph.D., Professor of *China University of Geosciences, Wuhan*, Email: zhaoej@cug.edu.cn

12 ^c Senior Engineer of *Haikou Marine Geological Survey Center*, Email: lxw1818168@163.com

13 ^d Assistant engineer of *Haikou Marine Geological Survey Center*, Email: 460305864@qq.com

14

15 Abstract

16 This study presents an integrated sand transport model that accounts for both wave and
17 current actions, along with non-constant grain properties, to investigate sediment dynamics in the
18 lower reaches of rivers. Taking the downstream and estuary of the Changhua River in Hainan
19 Island as a case study, topographic data and sediment sampling were conducted in the field,
20 complemented by remote sensing techniques. The model was rigorously validated using
21 theoretical and empirical methods, demonstrating excellent agreement with observed suspended
22 sediment concentrations at the Baoqiao Station. The findings indicate significant sediment
23 deposition in the estuary and lower reaches of the Changhua River, influenced by a combination
24 of hydrodynamic conditions and geological settings. Deposition in the estuary is primarily
25 affected by the northeast-southwest coastal currents and wave action, while deposition in the
26 river channel is associated with river constriction and variations in flow velocity. Regardless of
27 whether it is the dry or wet season, the residual current in the study area flows towards Beili Bay,
28 indicating that the sediment in the lower reaches of the Changhua River will be influenced by the
29 residual flow, moving southward.

30 **Keywords:** Sand transport model, Wave-current interaction, Non-constant sediment properties,
31 Changhua River, Hainan Island

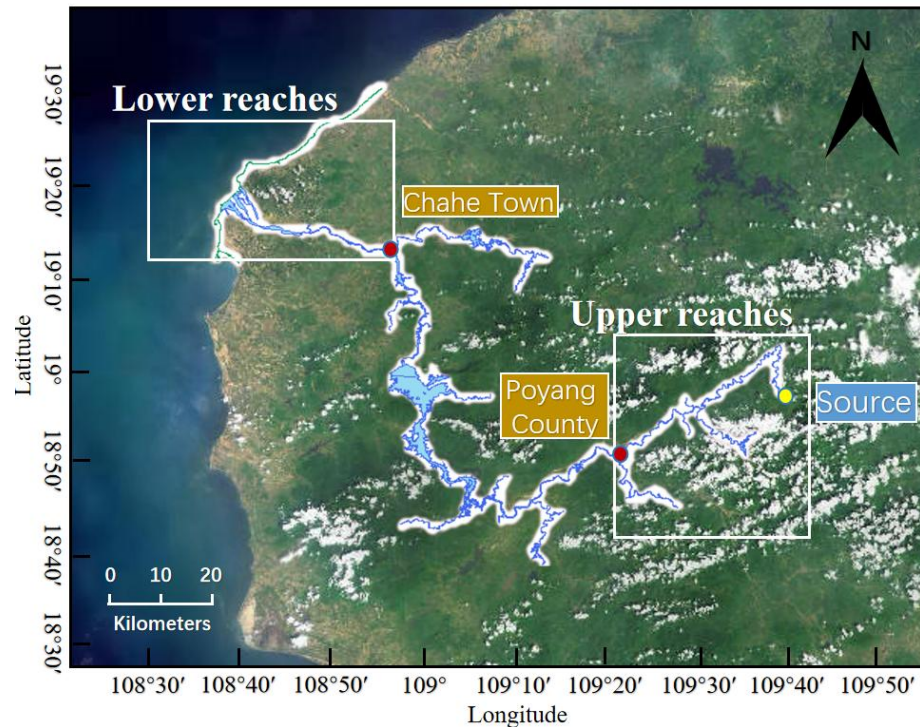
32 1. Introduction

33 Hainan Island has an extensive coastline, making marine economy a crucial source of its
34 economic prosperity (Feng et al., 2021, Jin et al., 2008, Fang et al., 2021). Changhua River is the
35 second largest river in Hainan in terms of its basin area (Zhang et al., 2020, Zeng and Zeng,
36 1989), which flowing uniquely into the Beibu Gulf in the northwest of Hainan Island, serves as a

删除[Yuxi Wu]: The models and methods developed in this study provide a scientific basis for sediment management and coastal evolution in similar downstream riverine environments and discuss the feasible scheme of sediment control in the downstream of Changhua River.

删除[Yuxi Wu]: **Plain language significance statement**
This study develops an integrated sand transport model to explore sediment dynamics in river downstream, focusing on the Changhua River estuary in Hainan Island. The research is crucial as it addresses the complex interplay between waves, currents, and sediment movement, key to estuarine ecosystems and shoreline changes. Our model, verified with field data, reveals significant sediment deposition patterns influenced by coastal currents and geological features. The findings are vital for coastal management, offering insights into how sedimentation can be monitored and controlled. This work suggests that similar models could be applied to other river systems, potentially guiding sustainable coastal development and protection strategies.

37 crucial water source for the region, supporting irrigation, power generation, and water supply
38 (Yang et al., 2013, Wang et al., 2023). The Changhua River is divided into upper, middle, and
39 lower reaches based on its natural geographical characteristics: the upper reaches extend from
40 the source to Poyang with a length of 79 kilometers and an average gradient of 14.87 %; the
41 middle reaches run from Poyang to Chahe with a total length of 84 kilometers, which includes a
42 significant drop at Guangba in Dongfang County, and generally feature a milder gradient; the
43 lower reaches start from Chahe down to the river's mouth at Changhua Port, spanning 39
44 kilometers with an average gradient of 0.41 %, leading to a broad river plain (Figure 1).
45 Characterized by a gentler gradient and slower flow, the lower reaches are where the river's
46 capacity to carry sediment decreases, leading to increased sediment deposition. Currently, the
47 issues related to water and sediment in the lower reaches of Changhua River are primarily
48 divided into studies on sediment composition and sediment transport (Zhang et al., 2006, Wu et
49 al., 2012, Zhu et al., 2020, Gao et al., 2014, Wang et al., 2022, Zhao et al., 2021). About the
50 sediment concentration information, the annual sediment concentration of the Changhua River is
51 recorded as 0.173 kg/m³, with an average annual sediment discharge of 782,000 tons, classifying
52 it as a river with relatively low sediment load. From 2013 to 2021, the average sediment
53 concentration at Baoqiao Station in the lower reaches of the Changhua River was determined to
54 be 0.1227143 kg/m³.



55

56 **Figure 1** Division of the Upper, Middle, and Lower Reaches of the Changhua River (map origination:
 57 <https://hainan.tianditu.gov.cn/>)

58 In the lower reaches of rivers, sediment dynamics are influenced by both water flow and
 59 waves, which are crucial for understanding the changes in estuarine and nearshore ecosystems,
 60 shoreline evolution, and the development of ocean resources. With the rapid advancement of
 61 computational technologies, significant progress has been made in sediment modeling studies,
 62 particularly in modeling sediment transport in the lower reaches of rivers where wave and
 63 current interactions are considered.

64 Researchers have developed a variety of computational models to simulate sediment
 65 transport processes in the lower reaches. These models include one-dimensional (1D),
 66 two-dimensional (2D), and three-dimensional (3D) hydrodynamic and sediment transport models
 67 that describe the flow and sediment movement in rivers, lakes, and coastal areas (Papanicolaou et
 68 al., 2010). 1D models are typically used for large-scale, long-term sediment transport issues

69 (Thomas and Prashum, 1977, Holly and Rahuel, 1990, Papanicolaou et al., 2004), while 2D and
70 3D models are more suitable for simulating specific flow and sediment transport conditions,
71 especially in the lower reaches and estuary areas (Lee et al., 1997, Jia and Wang, 1999, Gessler et
72 al., 1999, Wu et al., 2000, Blumberg and Mellor, 1987).

73 Traditional sediment transport models have predominantly focused on the dynamics of
74 water flow, with wave action often addressed in a simplified manner or neglected altogether
75 (Bakhtyar et al., 2009, Lee et al., 1997, Spasojevic and Holly, 1990, Bai et al., 2017). We need
76 more accurate and comprehensive models that can describe and predict sediment behavior under
77 the combined action of waves and currents, especially for rivers with low sediment concentration.
78 In this context, the Van Rijn formula emerges as a critical tool for enhancing the precision of
79 sediment transport modeling (Van-Rijn, 1984). Originally formulated to calculate the transport of
80 bed load and suspended sediment, the Van Rijn formula has been adapted over time to
81 accommodate the intricate interplay between waves and currents. Its empirical nature, grounded
82 in extensive field and laboratory data, allows for a nuanced representation of sediment dynamics
83 in coastal environments. The recent applications of the Van Rijn formula in computational
84 models have further expanded its utility, providing a robust framework for analyzing sediment
85 behavior in scenarios characterized by wave and current interactions (Chen et al., 2024, Michel
86 et al., 2023, Addison – Atkinson et al., 2024).

87 With the advancement of computational technologies and the development of remote
88 sensing techniques, researchers have begun to incorporate the complex interactions of waves and
89 currents into sediment transport modeling (Han et al., 2022, Liu et al., 2014, Vinzon et al., 2023).
90 These models not only consider the velocity and direction of water flow but also account for the

91 energy input from waves, wave form changes, and the shear forces generated by wave-current
92 interactions. Studies have shown that sediment movement under wave action is not only
93 influenced by the shear stress of the water flow but also by the liquefaction and mass transport of
94 bottom sediment caused by waves (Niu et al., 2023). Additionally, the physical properties of
95 sediment, such as particle size distribution, concentration, and sedimentation rates, are crucial
96 factors affecting sediment behavior under the combined influence of waves and currents
97 (Constant et al., 2023, Salgado Terêncio et al., 2023).

98 Despite the progress made, sediment modeling under the combined action of waves and
99 currents still faces many challenges. For example, how to better simulate sediment transport in
100 complex turbulent flows, the coupling of flow and sediment transport, and the transport of
101 non-uniform sediment still require further research. Moreover, model input and calibration also
102 require more field data and experimental validation to ensure the reliability and applicability of
103 the models. To verify the effectiveness of wave-current coupled sediment model in rivers with
104 low sediment concentration, we take Changhua River in Hainan Province as an example to verify
105 it.

106 To sum up, the sediment simulation considering only water flow can no longer meet the
107 accuracy of sediment prediction, and there are still limitations in the verification of sediment
108 simulation considering the interaction of waves and water flow. Most river sediment models do
109 not study rivers with small sediment concentration separately and lack in-situ observation, so the
110 accuracy of the models needs further verification. Additionally, due to the small scope of the
111 lower reaches of Changhua River, the existing terrain extraction methods are not enough to
112 provide terrain data with appropriate accuracy. Moreover, the sediment concentration of

113 Changhua River is not large and the existing research data are limited. In the absence of
 114 topographic data and sediment data, a complete and mature sediment transport model has not
 115 been established in the lower reaches of Changhua River so far. In this paper, we take Changhua
 116 River in Hainan Province as a representative of the river with less sediment, and consider the
 117 sediment deposition under the combined action of waves and currents. Based on the measured
 118 topographic data and sediment sampling data, the bed load and suspended sediment load are
 119 calculated respectively by Van Rijn model, and the sediment model is established. The sediment
 120 transport rate method and in-situ observation of suspended sediment concentration are used to
 121 verify the model and analyze the sediment deposition in the lower reaches channel and estuary.

122 2. Research Methods

123 2.1 Combined Wave and Current Sand Transport Model

124 This study assumes the sediment to be non-viscous, and the sediment deposition model
 125 utilizes the results from the hydrodynamic model as open boundary driving forces. The model
 126 definition in the sand transport model is assumed as combined current and waves, calculating the
 127 bed load and suspended load separately. Bed load typically occurs close to the bed, while
 128 suspended load can be transported at various levels within the water column. Sediment particles
 129 begin to move and may become suspended when the bed shear stress exerted by waves and
 130 currents exceeds a critical threshold. The equations adopt Van Rijn model. Van Rijn proposed the
 131 following models for sediment transport of bed load and suspended load, which are suitable for
 132 sediment transport calculation under wave action (Van Rijn, 1984). The Van Rijn model formula

删除[Yuxi Wu]: The ocean hydrodynamic simulation in this study is based on the solution of the three-dimensional incompressible Reynolds-averaged Navier-Stokes equations, with adherence to the Boussinesq and hydrostatic pressure assumptions, namely the shallow water equations. The specific governing equations are as follows:

$$\frac{\partial h}{\partial t} + \frac{\partial(h\bar{u})}{\partial x} + \frac{\partial(h\bar{v})}{\partial y} = hS$$

(1)

$$\frac{\partial h\bar{u}}{\partial t} + \frac{\partial h\bar{u}^2}{\partial x} + \frac{\partial h\bar{u}\bar{v}}{\partial y} = -f\bar{v}h - gh\frac{\partial\eta}{\partial x} - \frac{h}{\rho_0}\frac{\partial p_a}{\partial x} - \frac{gh^2}{2\rho_0}\frac{\partial\rho}{\partial x} +$$

(2)

$$\frac{\partial h\bar{v}}{\partial t} + \frac{\partial h\bar{u}\bar{v}}{\partial x} + \frac{\partial h\bar{v}^2}{\partial y} = f\bar{u}h - gh\frac{\partial\eta}{\partial y} - \frac{h}{\rho_0}\frac{\partial p_a}{\partial y} - \frac{gh^2}{2\rho_0}\frac{\partial\rho}{\partial y} +$$

(3)

$$T_{xx} = 2A\frac{\partial\bar{u}}{\partial x}, \quad T_{xy} = A\left(\frac{\partial\bar{u}}{\partial y} + \frac{\partial\bar{v}}{\partial x}\right),$$

$$T_{yy} = 2A\frac{\partial\bar{v}}{\partial y}$$

(4)

Where t is time; x and y are Cartesian coordinates; η is water level; d is static water depth; h is total water depth ($h = \eta + d$); u and v are velocity components in the x and y directions, respectively; f is Coriolis coefficient, where f represents the latitude and denotes the Earth's angular rotation speed; g is acceleration due to gravity; ρ is density of water; τ is components of radiative stress; S is source-sink term;

$S_{xy}, S_{xx}, S_{yx}, S_{yy}$ are components of the radiation stress

tensor; T_{ij} is the lateral stresses include viscous friction, turbulent friction and differential advection.

133 is derived based on a set of variables that are crucial for understanding sediment transport
 134 dynamics, particularly in the context of rivers and coastal waters. These variables include:

$$q_s = f_{sl} \cdot C_a \cdot u_*^2 \quad (5)$$

$$q_b = 0.053 \frac{M^{2.1}}{D_*^{0.3}} \sqrt{(s-1)g \cdot d_{50}^3} \quad (6)$$

$$f_{sl} = C' \cdot \left(\frac{u_*}{u_s} \right)^m \quad (7)$$

$$u_* = \sqrt{\frac{\tau}{\rho}} \quad (8)$$

$$M = \left(\frac{u_{f'}}{u_{f,c}} \right) - 1 \quad (9)$$

$$u_{f,c} = \sqrt{\theta_c (s-1)g \cdot d_{50}} \quad (10)$$

$$u_{f'} = V \frac{\sqrt{g}}{C'} \quad (11)$$

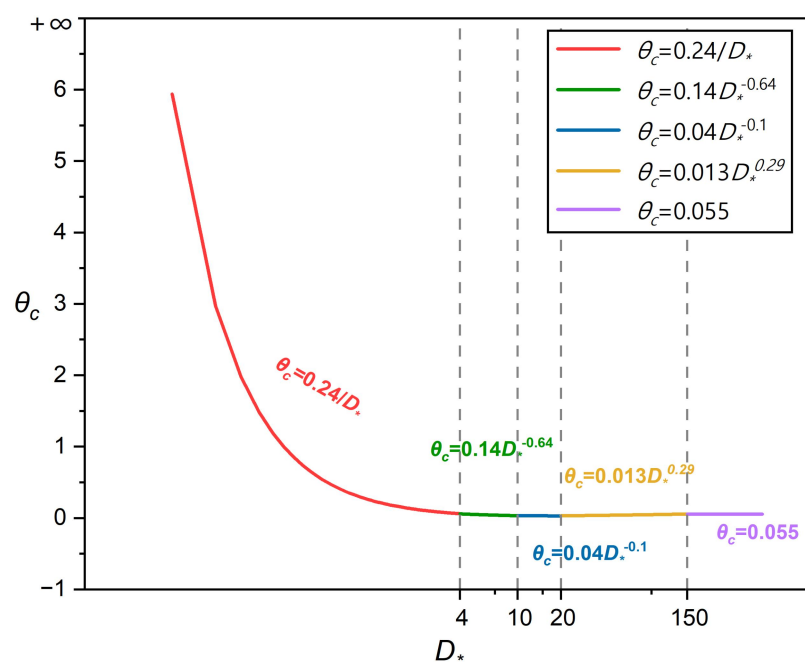
$$C' = 18 \log \left(\frac{4h}{d_{50}} \right) \quad (12)$$

$$D_* = d_{50} \sqrt[3]{\frac{(s-1)g}{\nu^2}} \quad (13)$$

135 Where q_b is the bed load transport rate; q_s is the suspended load transport rate; M is
 136 the non-dimensional transport stage parameter; $u_{f,c}$ is the critical friction velocity, which under
 137 the current; θ_c is the critical Shield parameter; $u_{f'}$ is the effective friction velocity; C' is the
 138 Chezy number originating from skin friction; D_* is the non-dimensional particle parameter;
 139 ν is the kinematic viscosity and approximately equal to 10^{-6} m²/s for water; C_a is the bed

140 concentration; u_* is the friction velocity; τ is the shear stress at the bed surface; ρ is the
 141 density of water; m is empirical exponent.

142 In the context of the Van Rijn model, the non-dimensional particle parameters can influence
 143 the value of the critical Shields parameter. For example, as the particle size increases, the critical
 144 Shields parameter may also increase because larger particles require more force to overcome
 145 gravity and initiate motion. Similarly, changes in fluid properties or flow conditions can affect
 146 both the non-dimensional particle parameters and the critical Shields parameter. Instead of using a
 147 constant critical Shields parameter θ_c , Van Rijn assumes the following variation as a function of
 148 D_* , see Figure 2.



149
 150 **Figure 2** Relations for determination of critical Shields stress

151 After calculating the bed load and suspended load separately, the Bijker model is used to
 152 calculate the total sediment transport rate (Bijker, E.W. 1967), which includes both bed load and
 153 suspended load components. and the formula is as follows:

$$q_t = q_s + q_b = q_b (1 + 1.83Q) \quad (14)$$

$$Q = A \left(\frac{I_1}{I_2} \right) + I_2 \ln \left(\frac{z^*}{r} \right) = \frac{h}{r} \left(\frac{I_1}{I_2} \right) + I_2 \ln \left(\frac{w}{rku_{f,wc}} \right) \quad (15)$$

$$u_{f,wc} = u_{f,c} + \sqrt{u_{f,c}^2 + 2 \cdot \frac{v^2}{V}} \quad (16)$$

$$I_1 = \int_0^h \frac{u(z)}{w} dz, \quad I_2 = \int_0^h \frac{u(z)}{w} \ln \left(\frac{h-z}{d_{50}} \right) dz, \quad (17)$$

154 Where q_t is the total sediment transport rate; Q is a dimensionless factor that accounts
 155 for the effect of waves on the bed load transport; h represents the water depth; r is the bed
 156 roughness; I_1 and I_2 are Einstein's integrals, which are functions of the dimensionless
 157 reference level A and the dimensionless roughness height z^* ; w is the settling velocity of the
 158 suspended sediment; k is von Karman's constant; $u_{f,wc}$ is the shear velocity under the
 159 influence of combined waves and current; v is the amplitude of the wave-induced oscillatory
 160 velocity at the bottom; V is the depth-averaged flow velocity; $u(z)$ is the flow velocity
 161 profile at a height z above the bed.

162 **2.2 Influences of Waves and Currents**

163 The influence of sediment transport model on water flow has been widely studied and
 164 applied ([Papanicolaou et al., 2010](#)), including sediment transport mechanisms, the establishment
 165 of the boundary layer, modifications to bed morphology, and the vertical distribution of
 166 suspended sediment. However, the theory and application of wave action are not mature
 167 compared with water flow. This chapter emphasizes the motion equation and boundary condition
 168 equation adopted by wave action in the sediment transport model in this paper.

169 The model of sediment transport to calculate the influence of the waves usually through a

170 comprehensive consideration of various factors that encapsulate the impact of waves on sediment
171 transport. The typical models incorporate the nonlinear characteristics of wave motion, net mass
172 transport induced by waves, turbulence generated by wave breaking, the temporal evolution of
173 the boundary layer due to combined wave and current action, contributions to turbulence from
174 three sources (wave boundary layer, mean flow, and wave breaking), and the influence of
175 wave-formed ripples on flow and sediment transport. A suite of wave theories, such as Stokes
176 and Cnoidal theories, are employed to describe wave motion across different hydrodynamic
177 conditions. Additionally, the model accounts for the calculation of turbulence viscosity due to
178 wave breaking, and the equations to compute the shear stress resulting from wave motion are
179 well represented. These complex interactions and processes are articulated through a series of
180 mathematical equations and empirical formulas, enabling the model to accurately simulate the
181 process of sediment transport under the dual influence of waves and current. In this paper, the
182 specific formulas of the wave motion are as follows:

183 **Table 1 Formulas of the wave motion in the sand transport model**

Item	Method	Equation
Wave Energy Dissipation	Battjes and Janssen (1978)	$D = \frac{\gamma_1 g H^2}{\gamma_2 k} \tanh(\gamma_2 kh)$
Wave Boundary Layer Thickness	Empirical formula	$\delta = \frac{k}{30} \left(\frac{u_{\max}}{u_*} \right)$
Turbulent Viscosity Induced by Waves	Empirical formula	$\nu_t = C_\mu \frac{u_{\max}^2}{g}$
Shear stress resulting from wave motion	Jørgen Fredsøe (1984)	$\tau = \rho u_*^2$
Wave velocity in shallow water	Cnoidal theory	$c = \sqrt{gh} \left[1 + \frac{H}{h} \left(\frac{1}{k^2} - 0.5 - \frac{3E(x)}{2k^2 K(x)} \right) \right]$ (k is the module of elliptic function. $E(x)$ and $K(x)$ are the first and second complete elliptic integrals)
Wave velocity in deep water	Stokes theory	$c = \sqrt{\frac{g\lambda}{2\pi}}$

184 After examining the influence of waves and currents on sediment transport modelling, we
185 now turn our attention to the specific characteristics of sediment properties in the study area.
186 Section 2.3 provides a detailed account of these properties, which are essential for understanding
187 the local sediment dynamics and will be crucial for the model's calibration and validation
188 processes.

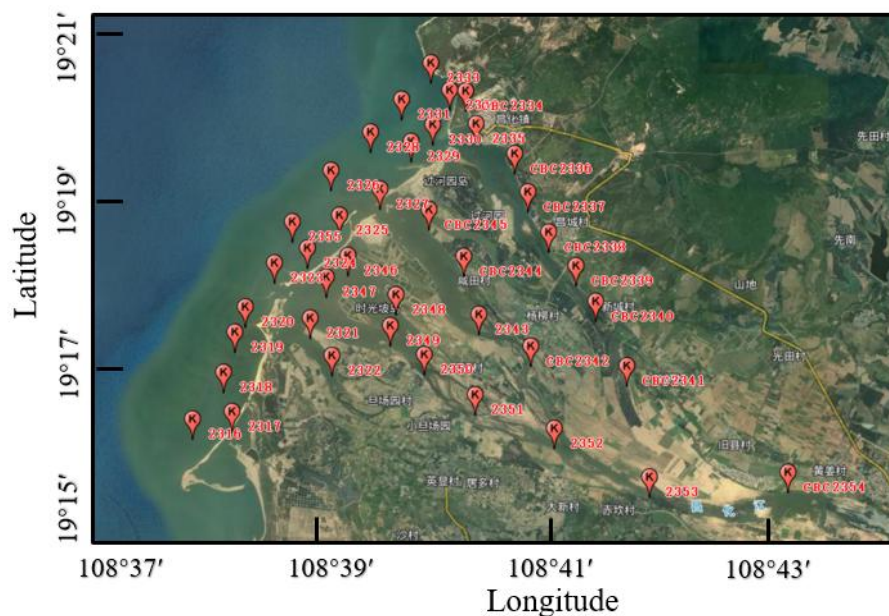
删除[Yuxi Wu]: Additionally the influence of waves and currents on the sediment transport model, sediment parameters are the direct conditions that affect the accuracy of the model, as follows.

189 **2.3 Non-constant sediment properties**

190 Generally speaking, sediment data may have different particle size, sorting, porosity and
191 relative density equivalence, and are not uniform. These characteristics lead to the increase of
192 computational complexity (Adnan et al., 2019), so most of studies set the sediment parameters in
193 the study area as a constant parameter for calculation (Mohd Salleh et al., 2024, Auguste et al.,
194 2021). Actually, the spatial distribution of sediment parameters is not constant. Seabed sediment
195 is not homogeneous, and as the distance from the shore increases, the grain size of the deposited
196 sediment continuously decreases. Some researches had proved the validity of sand transport
197 model with spatially variable sediment properties (Doroudi and Sharafati, 2024, Bui and Bui,
198 2020). Sediment properties can be obtained by direct method and indirect method. The indirect
199 method includes theoretical formula and empirical formula, while the direct method is sampling
200 (Claude et al., 2012, Leary and Buscombe, 2020). Studies had shown that indirect methods are
201 less effective than direct sampling (Claude et al., 2012). In this paper, sediment sampling is
202 conducted using a clam grab sampler to collect surface geological samples from targeted sea
203 areas. The study area is divided into river channel and estuary segments, with sediment samples
204 collected at consistent intervals (Figure 3). We sampled 15 points in estuary of the lower reaches
205 of Changhua River and 40 points in the channel. To ascertain sediment parameters, including

删除[Yuxi Wu]: riverway

206 grain size and sorting factors, a laser particle size analyzer is utilized.



207

208 **Figure 3** Location of sediment sampling point (map origination: <https://hainan.tianditu.gov.cn/>)

209 After selection, the analytical process detailed particle size and sediment segregation data
210 (Table 2 and Table 3). Grain size parameters are quantitative representations of the grain size
211 characteristics of the clastic material in terms of certain values. The individual grain size
212 parameters and their combined characteristics can be used as the basis for discriminating the
213 depositional hydrodynamic conditions and depositional environment. The commonly used
214 parameters are mean particle diameter (Mz), sorting coefficient (δ_i) and median grain diameter
215 (Φ_{50}). The number of samples at the estuary with a median grain diameter between 0 and 1ϕ is
216 9, accounting for 60 %; the number of samples with a mean grain size between 1ϕ and 3ϕ is 3,
217 accounting for 20 %; the number of samples with a median grain size between -1ϕ and 0 is 3,
218 accounting for 20 %. While, in the estuary and 40 points in the lower reaches, the number of
219 samples with a median grain diameter between 0 and 1ϕ is 24, accounting for 60 %; the number
220 of samples with a median grain size between 1ϕ and 3ϕ is 8, accounting for 20 %; the number

221 of samples with a median grain size between 3ϕ and 7ϕ is 7, accounting for 17.5 %; the

222 number of samples with a median grain size between -1ϕ and 0 is 1, accounting for 2.5 %.

223 **Table 2** Grain parameters of samples at the estuary

Number	Coefficient of granularity			Classification of sediments
	Mean grain diameter $Mz(\phi)$	Sorting factor δ_i	Median grain diameter $\Phi_{50}(\phi)$	
1	<0.04	0.7600	0.02	Gravel sand
2	<0.04	1.1000	-0.44	Sandy gravel
3	0.33	0.7600	0.33	Sand
4	<0.04	0.7900	0.01	Silty sand
5	0.50	0.7700	0.51	Sand
6	0.40	0.8200	0.41	Sand
7	0.98	0.6500	1.00	Sand
8	1.35	0.6900	1.41	Sand
9	2.91	0.9600	2.87	Sand
10	0.31	0.7700	0.32	Sand
11	0.26	0.7600	0.27	Sand
12	<0.04	0.6700	-0.41	Sandy gravel
13	<0.04	0.8000	-0.15	Silty sand
14	0.18	0.7700	0.19	Sand
15	0.70	1.2900	0.69	Sandy gravel

删除[Yuxi Wu]: (ϕ)

224 **Table 3** Grain parameters of samples of the river

Number	Content of grain (%)				Coefficient of granularity			Classification of sediments
	Gravel	Sand	Silt	Clay	Mean grain diameter $Mz(\phi)$	Sorting factor δ_i	Median grain diameter $\Phi_{50}(\phi)$	

删除[Yuxi Wu]: (ϕ)

1	0.00	8.55	83.90	7.55	6.01	1.42	6.09	Silt
2	0.00	70.64	26.48	2.88	3.33	2.14	2.44	Silty sand
3	0.00	85.98	13.06	0.96	2.82	1.26	2.79	Silty sand
4	0.00	87.44	6.38	0.45	2.64	1.27	2.57	Silty sand
5	5.90	93.12	0.98	0.00	0.15	0.75	0.16	Gravel sand
6	0.00	2.48	89.78	7.74	6.20	1.26	6.22	Silt
7	0.00	9.12	81.51	9.37	6.25	1.47	6.45	Silt
8	10.96	87.75	0.97	0.07	<0.04	0.70	-0.17	Gravel sand
9	1.18	98.02	0.75	0.05	0.51	0.72	0.52	Gravelly sand
10	8.18	90.50	1.21	0.11	0.12	0.84	0.11	Gravel sand
11	4.42	92.40	2.95	0.23	0.30	0.83	0.29	Gravelly sand
12	3.56	91.40	4.77	0.46	0.79	1.33	0.74	Gravelly sand
13	0.03	96.04	3.57	0.36	1.17	0.86	1.17	Gravelly sand
14	1.13	91.58	6.84	0.45	1.24	1.40	1.16	Gravelly sand
15	1.51	95.25	2.90	0.33	0.71	0.92	0.68	Gravelly sand
16	0.00	94.96	4.68	0.35	1.32	1.00	1.31	Sand
17	0.00	96.21	3.47	0.32	1.34	0.81	1.33	Sand
18	0.00	98.26	1.40	0.34	1.21	0.71	1.20	Sand
19	0.00	17.37	74.44	8.20	5.89	1.81	6.33	Sandy silt
20	0.00	1.61	89.02	9.37	6.33	1.27	6.39	Silt
21	4.70	47.88	42.65	4.52	3.43	3.20	3.69	Gravelly muddy sand
22	28.43	71.40	0.12	0.05	0.69	0.84	0.75	Gravel sand
23	4.01	45.93	44.98	5.07	3.57	3.19	3.99	Gravelly mud
24	3.26	75.71	20.00	1.42	1.77	2.53	0.63	Gravelly muddy sand
25	0.05	98.99	0.88	0.08	0.91	0.70	0.92	Gravelly sand
26	2.86	91.07	5.73	0.34	0.67	1.29	0.62	Gravelly sand
27	40.14	60.58	14.52	1.16	1.54	2.66	0.39	Muddy sandy gravel

28	24.57	69.98	4.97	0.47	0.13	1.43	0.11	Gravel sand
29	26.79	69.74	3.26	0.21	0.56	0.99	0.55	Gravel sand
30	36.45	72.08	4.72	0.40	0.21	1.35	0.22	Sandy gravel
31	5.23	92.23	2.34	0.20	0.30	0.83	0.30	Gravel sand
32	0.79	99.21	0.00	0.00	0.73	0.75	0.75	Gravelly sand
33	4.06	95.54	0.68	0.08	0.44	0.82	0.47	Gravelly sand
34	17.53	73.84	8.00	0.63	0.36	1.59	0.29	Gravelly muddy sand
35	0.85	99.15	0.00	0.00	0.64	0.72	0.65	Gravelly sand
36	38.74	67.26	9.86	0.98	0.58	1.82	0.33	Muddy sandy gravel
37	32.10	51.01	15.89	1.01	1.61	2.73	0.26	Muddy sandy gravel
38	52.91	34.33	11.76	1.01	1.64	2.91	0.07	Muddy sandy gravel
39	7.23	72.16	19.53	1.07	1.46	2.53	0.38	Gravelly muddy sand
40	3.81	90.24	4.21	0.37	0.38	0.94	0.45	Gravelly sand

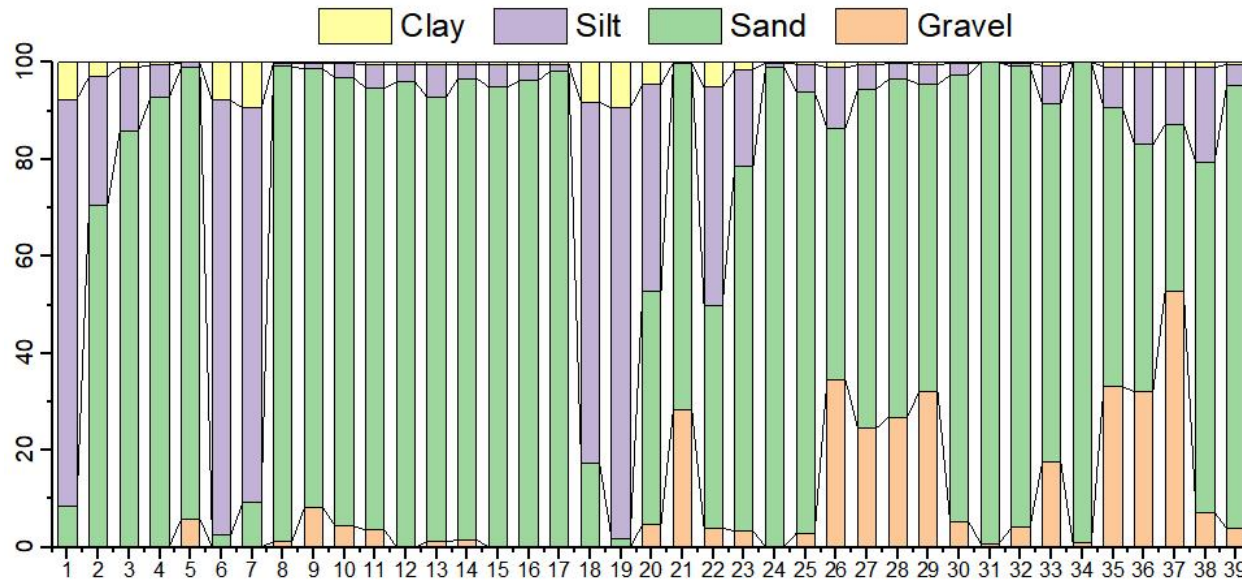
225 The surface sediment particles in the nearshore area of Changhua river course are mainly
226 divided into three grain size components, gravel (>2 mm), sand (0.063~2 mm), silt (0.004~0.063
227 mm), with relative percentages of 9.28%, 72.18% and 18.54%, respectively. Based on the
228 sampling and testing results of the river course, we can obtain the histogram of the component
229 percentage for each sample (Figure 4). It is obvious that the sediment composition in the river
230 channel is dominated by sand, followed by silt.

删除[Yuxi Wu]: 2

删除[Yuxi Wu]: 0.063

删除[Yuxi Wu]: 0.063

删除[Yuxi Wu]: 0.004



231

232

Figure 4 Percentage composition of components in river samples

233

According to the classification criteria of the sorting coefficients by Focke–Ward (Table 4),

234 Sediments from the Changhua River estuary in the lower reaches exhibit medium sorting with

235 coefficients of most samples between 0.71~1.00 and a median grain diameter predominantly

236 under 1.5 mm, characterized mainly by sand. In contrast, sediments within the river stretch

237 between Baoqiao Station and the lower reaches are coarser with poorer sorting, evidenced by a

238 sorting coefficient exceeding 1.00 in 23 out of 40 samples (over 57 %).

239

Table 4 Sorting level table

Sorting Grade	Sorting factor (δ_i)
Sorting excellent	<0.35
Sorting good	0.35~0.71
Sorting medium	0.71~1.00
Sorting poor	1.00~4.00

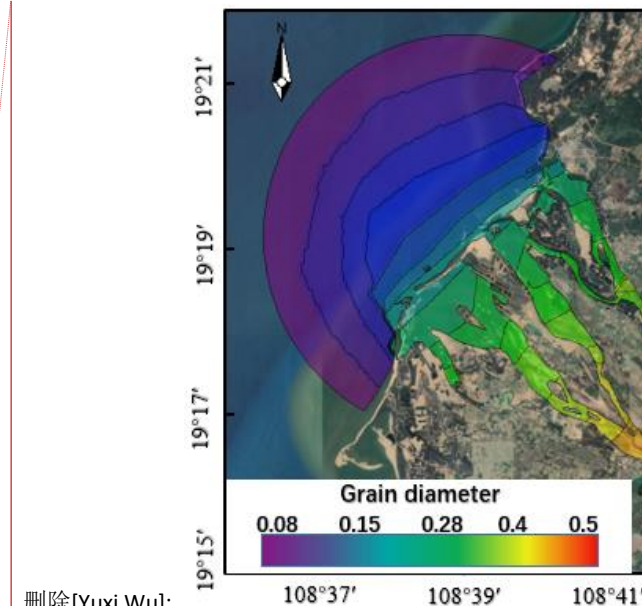
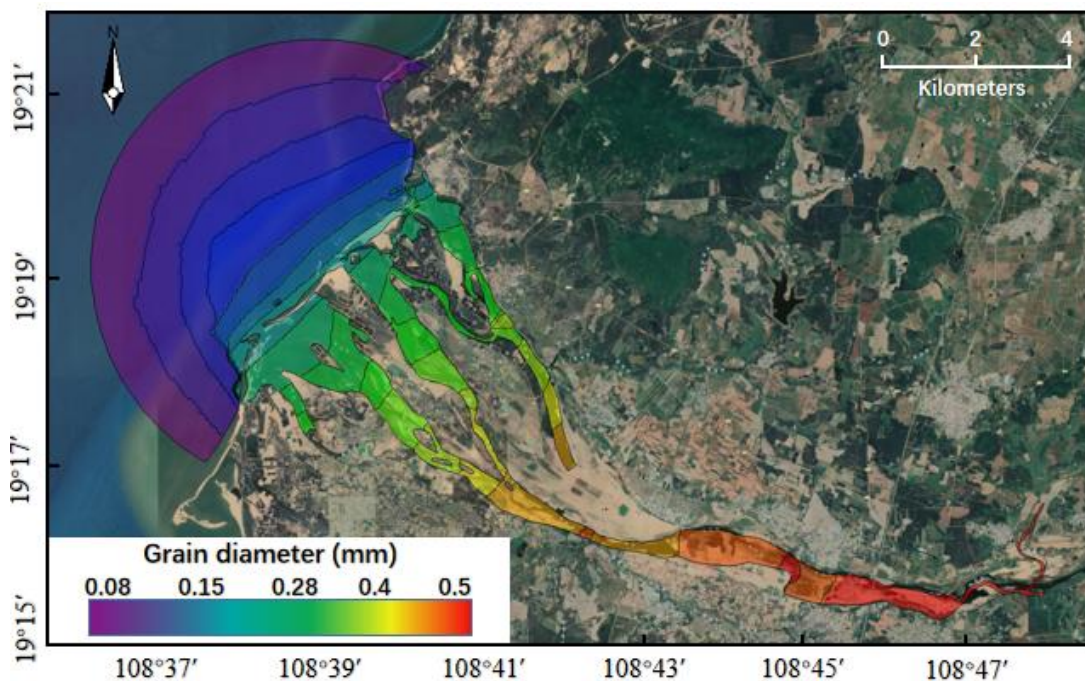
删除[Yuxi Wu]: (φ)

240 To ascertain the sediment composition and the dry bulk density in the estuary, 15 samples

241 were collected from the Changhua River estuary. These samples were dried to measure mass and

242 volume, thereby determining the dry bulk density of the sediment. After calculating, the dry bulk

243 density is 1210.9 kg/m³ which used in sand transport model. This analysis is crucial for model
 244 accuracy and understanding sediment behavior in the estuarine environment. According to the
 245 sampling position, the research area is divided into areas. After sorting and interpolation, the
 246 spatial variation of sediment particle size data and sorting data in the study area are obtained
 247 (Figure 5).



删除[Yuxi Wu]:

删除[Yuxi Wu]: Two-dimensional spatial v

248

249 **Figure 5** Variation of sediment particle size data (map origination: <https://hainan.tianditu.gov.cn/>)

250 2.4 Reliability evaluation index

251 In this paper, Nash-Sutcliffe model efficiency coefficient (NSE) and root mean squared
 252 error (RMSE) are used to evaluate the reliability of the model. The calculation formulas (Nash
 253 and Sutcliffe, 1970) are as follows:

$$NSE = 1 - \frac{\sum_{i=1}^N (M_i - O_i)^2}{\sum_{i=1}^N (O_i - \bar{O})^2} \quad (17)$$

$$RMSE = \sqrt{\frac{\sum_{i=1}^N (M_i - O_i)^2}{N}} \quad (18)$$

254 In Equations: M_i is the model simulation value at the i moment; O_i is the measured value at
 255 the i moment; \bar{O} is the average of the measured values of the site at all simulation moments; N
 256 is the total number of all simulation moments. Among them, the value range of NSE is 0~1.
 257 When $0.65 \leq NSE < 1$, the fitting degree of the model is excellent; When $0.5 \leq NSE < 0.65$, the
 258 fitting degree of the model is good; When $0.2 \leq NSE < 0.5$, the fitting degree of the model is
 259 general; When $0 < NSE < 0.2$, the fitting degree of the model is poor.

260 **3. Model Region and Settings**

删除[Yuxi Wu]: Example in the lower reaches of the Changhua River

261 The study area is situated in the western part of Hainan Island, mainly encompassing the
 262 lower reaches of Changhua River and its estuary. The approximate coordinates range from
 263 $108^{\circ}36'E$ to $108^{\circ}50'E$ and $19^{\circ}15'N$ to $19^{\circ}22'N$. The study area covers a large part of the region
 264 from Chahe Town to the estuary of the Changhua River, including towns such as Changhua
 265 Town, Sigeng Town, Sanjia Town, and Wulie Town, among others. An unstructured grid, finite
 266 volume, regional ocean model FVCOM (Chen et al., 2003) was used to simulate the
 267 hydrodynamic background and hydrological features. It has been widely used for the study of
 268 coastal oceanic and estuarine circulation (Jiang and Xia, 2016; Huang et al., 2008; Lai et al.,
 269 2018; Chen et al., 2008). The model's open boundary relies on forced tidal level data extracted
 270 using the Earth and Space Research's (ESR) Matlab "Tide Model Driver" (TMD) toolbox
 271 (<https://www.esr.org/research/polar-tide-models/tmd-software/>) from the TPXO 6.2 global tidal
 272 wave prediction model.

删除[Yuxi Wu]: 3.1 Model Region

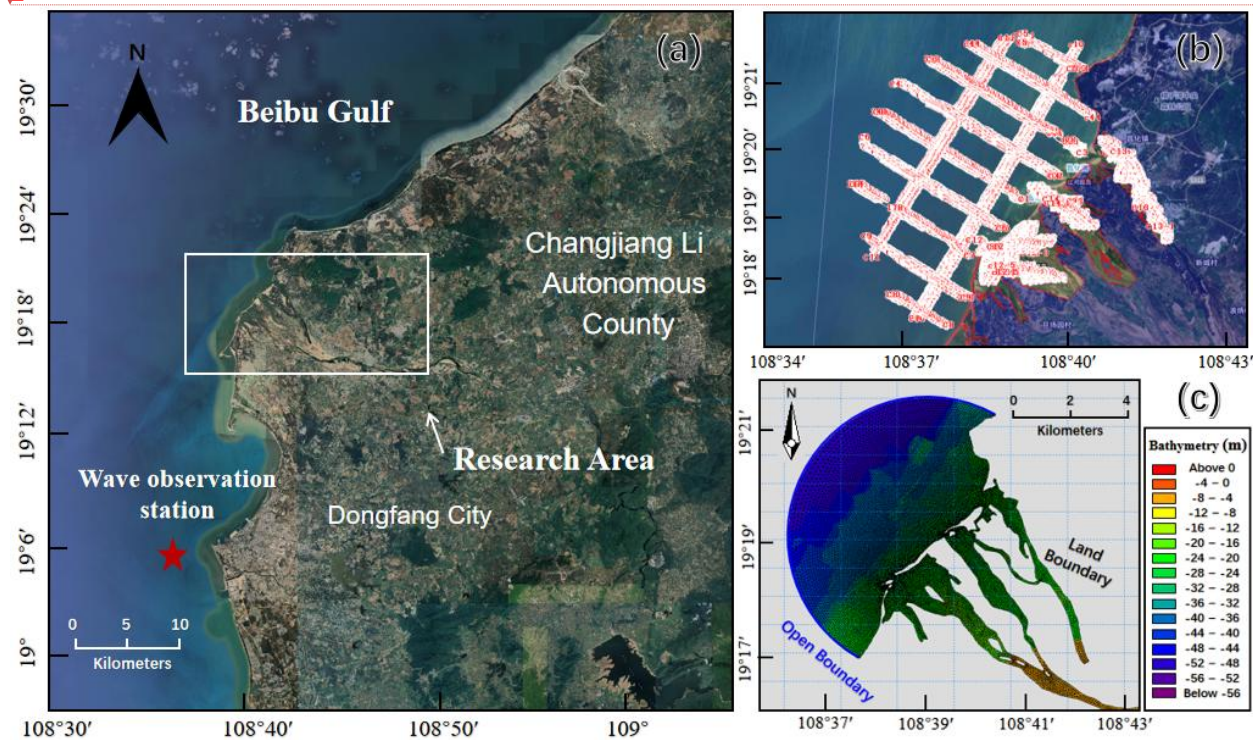
设置格式[Yuxi Wu]: 字体颜色: 蓝色

设置格式[Yuxi Wu]: 字体颜色: 蓝色

设置格式[Yuxi Wu]: 字体颜色: 蓝色

设置格式[Yuxi Wu]: 图案: 清除(白色), 字距调整: 1 磅, 英语(美国), (中文) 德语(德国)

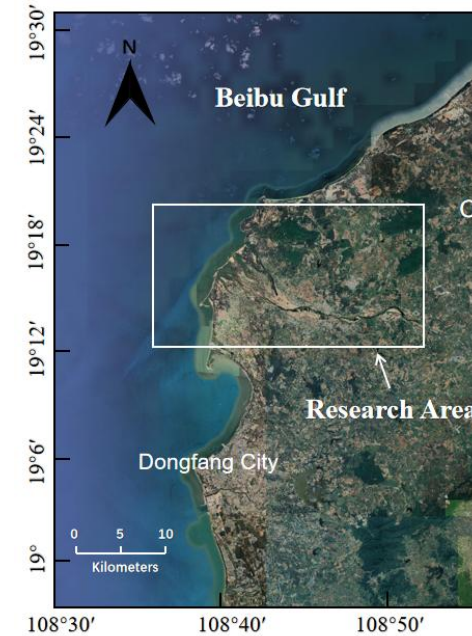
273



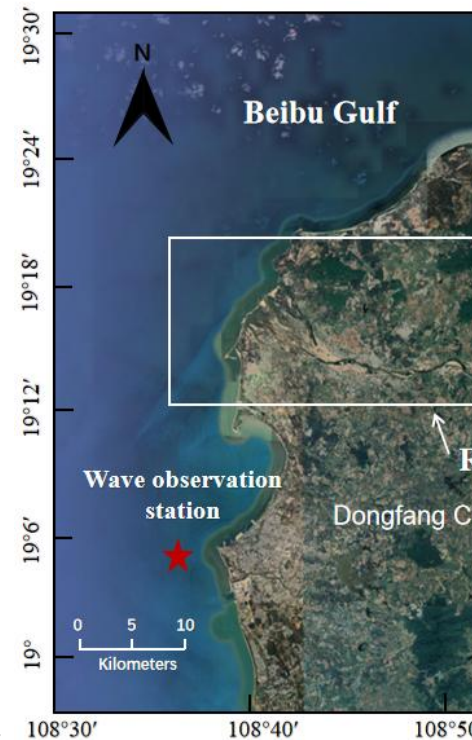
274

275 **Figure 6** (a) Scope of study area (the white frame) and wave observation (the red star) from Dongfang; (b)
 276 ADCP collection points on site; (c) Grids and boundaries (map origination:
 277 <https://hainan.tianditu.gov.cn/>)

278 In the study, bathymetric data is derived from ETOPO1 global seafloor topography data and
 279 in-situ measurements using ADCP. The spatial resolution of ETOPO1 data is $1/60^\circ \times 1/60^\circ$,
 280 which is insufficient for the research requirements. ADCP depth measurements have higher
 281 density in nearshore areas and provide actual measured data with higher accuracy. The model
 282 employs a triangular unstructured grid. To enhance computational accuracy and reduce
 283 computation time, the density of boundary nodes gradually decreases from nearshore to offshore.
 284 In the offshore region, the grid density is lower, with a resolution of 0.25 km, while the nearshore
 285 part of the open boundary has higher grid resolution. In the main research area near the river
 286 channel, the grid resolution is highest, reaching 25 m. The entire study area grid comprises a total
 287 of 13, 814 computational nodes. The wave parameters at the open boundary are set to fixed



删除[Yuxi Wu]:



删除[Yuxi Wu]:

删除[Yuxi Wu]: (The right figure shows the 3D terrain after the interpolation of ETOPO1 topographic data, the red dots are the original data.)

288 values, referring to the annual average frequency of occurrence of wave heights in various
289 directions at the Dongfang Ocean Station over the years (Ding, 1990, Hu, 2009, Wang, 2023).

290 The model's open boundary conditions are defined by the forced tidal water level,
291 incorporating eight primary tidal components: M2, S2, K1, O1, N2, K2, P1, and Q1. The model's
292 closed boundary aligns with the terrestrial boundary, where the normal velocity of ocean currents
293 is set to zero, precluding any exchange of temperature and salt between land and seawater. The
294 time resolution of tidal level data is 1 hour and the accuracy is 1 cm. There are 121 open
295 boundary control points. The model also integrates the impact of wind fields, with data sourced
296 from ECMWF at a resolution of $1/8^\circ \times 1/8^\circ$. This dataset encompasses the u (east-west) and v
297 (north-south) components of the wind vector, along with sea level pressure. The upper boundary
298 of the model is set based on the multi-year average monthly flow and sediment concentration
299 data from the Baoqiao Hydrological Station in Chahe Town. The upstream boundary is assigned
300 a flow rate of $44 \text{ m}^3/\text{s}$, and the suspended sediment concentration is set at $5 \text{ g}/\text{m}^3$. The median
301 grain size and sorting coefficient of the initial sediment distribution are determined through the
302 partitioning based on the measured sediment data from Section 2.3. The porosity is set to 0.4,
303 and the sediment density is $2650 \text{ kg}/\text{m}^3$. In this study, we calibrated the hydrodynamic model
304 using water level data from April and May of 2022. The data were collected from Basuo port
305 station. One-At-a-Time (OAT/OFAT) method (Czitrom, 1999) is used to modify the parameters,
306 an effective local sensitivity analysis technique. In each experiment, we alter one factors while
307 holding the others constant. During the calibration process, our primary focus was on the model's
308 hydrodynamic response. This was achieved by adjusting the flow resistance parameters and the
309 bed roughness coefficients within the model. The calibrated model parameters are presented in
310 Table 5.

删除[Yuxi Wu]: For the setup of wave conditions, this paper selects the JONSWAP spectrum for the initial condition spectrum of the boundary. The wave parameters at the open boundary are set to fixed values, referring to the annual average frequency of occurrence of wave heights in various directions at the Dongfang Ocean Station over the years, as well as the number of days and frequency of occurrence in different seasons for each wave level (Ding, 1990, Hu, 2009, Wang, 2023). The wave field are driven by wind, with reference to the 10-meter wind speed and pressure parameters from the ERA5 reanalysis data provided by European Centre for Medium-Range Weather Forecasts (ECMWF).

设置格式[Yuxi Wu]: 字体颜色: 蓝色

删除[Yuxi Wu]: After introducing these environmental conditions into the model, a hydrodynamic model containing water level and flow information can be obtained.

设置格式[Yuxi Wu]: 上标

设置格式[Yuxi Wu]: 上标

删除[Yuxi Wu]: A detailed description of all parameters employed in the hydrodynamic model is provided in Table 2.

设置格式[Yuxi Wu]: 字体颜色: 蓝色

311

Table 5 Parameters of the hydrodynamic model

<u>Parameter</u>	<u>Value</u>
<u>Shoreline</u>	<u>GSHHS</u>
<u>Bathymetry</u>	<u>ETOPO1 and ADCP in-situ</u>
<u>Grid</u>	<u>0.25 km at the boundaries to 25 m near the coastline</u>
<u>Time period</u>	<u>23/4/2023 00:00-30/4/2023 00:00 (Low water period)</u> <u>28/6/2022 00:00-1/8/2022 00:00 (High water period)</u>
<u>Manning number</u>	<u>28</u>
<u>Eddy viscosity</u>	<u>Smagorinsky formulation data 0.28 m²/s</u>
<u>Time step</u>	<u>300 s</u>
<u>Tidal constituents</u>	<u>M2, S2, K1, O1, N2, K2, P1, Q1</u>
<u>Wind/Sea level Pressure</u>	<u>ERA 5</u>
<u>Validation</u>	<u>Basuo Port Station (19°06' N, 108°37' E)</u>

312 Considering the limitations of the FVCOM model in wave calculations, this study selects
313 the widely-used third-generation SWAN model for numerical simulation of wind waves in this
314 region. The wave field are driven by wind and current from hydrodynamic model. The
315 parameters used in the model setups are based on the values listed in Table 6. The wave model at
316 the open boundary is defined by the JONSWAP spectrum, with a spectral resolution of 40
317 frequency bins and 36 directional sectors. Calibrate the parameters using multi-year wave data
318 from the Dongfang Ocean Station. The directional resolution is set to 40 sectors, with a particular
319 focus on the southwest (SSW) and southwest (SW) directions where the waves are most frequent.
320 The wind speed and wind direction are from the ERA5 reanalysis data provided by ECMWF.
321 The peak parameter (γ) of the JONSWAP spectrum, indicative of the wave asymmetry, was
322 specified at 3.3, and the spectral width parameter was set to 0.07 to define the shape of the wave
323 spectrum.

324

Table 6 Parameters of the wave model

设置格式[Yuxi Wu]: 字体: (默认) Times New Roman

设置格式[Yuxi Wu]: 字体: (默认) Palatino Linotype, 10 磅,
字体颜色: 黑色

设置格式[Yuxi Wu]: 字体: (默认) Times New Roman

设置格式[Yuxi Wu]: 字体: (中文) 等线, (中文) 中文(简体)

设置格式[Yuxi Wu]: 字体: (中文) 等线, (中文) 中文(简体)

设置格式[Yuxi Wu]: 字体: (默认) Palatino Linotype, (中
文) Times New Roman, 10 磅

设置格式[Yuxi Wu]: 字体: (默认) Palatino Linotype, (中
文) Times New Roman, 10 磅

设置格式[Yuxi Wu]: 字体: (默认) Palatino Linotype, (中
文) Times New Roman, 10 磅, (中文) 德语(德国)

设置格式[Yuxi Wu]: 字体: (默认) Palatino Linotype, (中
文) Times New Roman, 10 磅

设置格式[Yuxi Wu]: 字体: (默认) Palatino Linotype, (中
文) Times New Roman, 10 磅, (中文) 德语(德国)

设置格式[Yuxi Wu]: 字体: (默认) Palatino Linotype, (中
文) Times New Roman, 10 磅

删除[Yuxi Wu]: , and given the significant impact of wind
waves on the hydrodynamics characteristics in the Tieshan
Bay area,

<u>Parameter</u>	<u>Value</u>
<u>Whitecapping dissipation (C_{ds})</u>	<u>2.36×10^{-5}</u>
<u>Pierson-Moskowitz (S_{pm})</u>	<u>3.02×10^{-5}</u>
<u>Dissipation (α)</u>	<u>1.0</u>
<u>Breaking index (γ)</u>	<u>0.73</u>
<u>JONSWAP formulation (C_{bottom})</u>	<u>0.067</u>

325 A mathematical model established through a wave-current coupling approach can accurately
326 describe the motion laws of wave-generated currents and consider the impact of nearshore
327 currents on wave propagation. It also reflects the interaction between nearshore waves and
328 currents. In this paper, a three-dimensional sediment transport model is constructed using the
329 model coupler MCT to perform real-time coupling between the hydrodynamic model FVCOM
330 and the wave model SWAN, employing the same unstructured grid for the coupling (Chen et al.,
331 2018; Ji et al., 2022). The coupling process can be summarized as follows: the FVCOM
332 hydrodynamic model and the SWAN wave model transmit the calculated three-dimensional flow
333 field and wave data to the sediment module, which then calculates the suspended and bed load
334 sediment transport rates, achieving data linkage between the three-dimensional wave-current
335 coupled model and the sediment transport model.

336 4. Hydrodynamic Model

337 4.1 Verification of hydrodynamic model

338 In order to ensure the validity of the model, the tidal current data of one tide gauge station
339 and two ADCP points in the study area are compared and verified. Figure 7 shows the hourly
340 water level comparison between the measured tidal water level at Basuo Port Station (19°06'N,

设置格式[Yuxi Wu]: 下标

设置格式[Yuxi Wu]: 上标

设置格式[Yuxi Wu]: 下标

设置格式[Yuxi Wu]: 字体: 小五

带格式表格[Yuxi Wu]

设置格式[Yuxi Wu]: 字体: (中文)等线, (中文)中文(简体)

设置格式[Yuxi Wu]: 下标

设置格式[Yuxi Wu]: 字体颜色: 蓝色

设置格式[Yuxi Wu]: Heading-Main, 缩进: 首行缩进: 0 字符, 段落间距段前: 24 磅, 行距: 2 倍行距, 图案: 清除

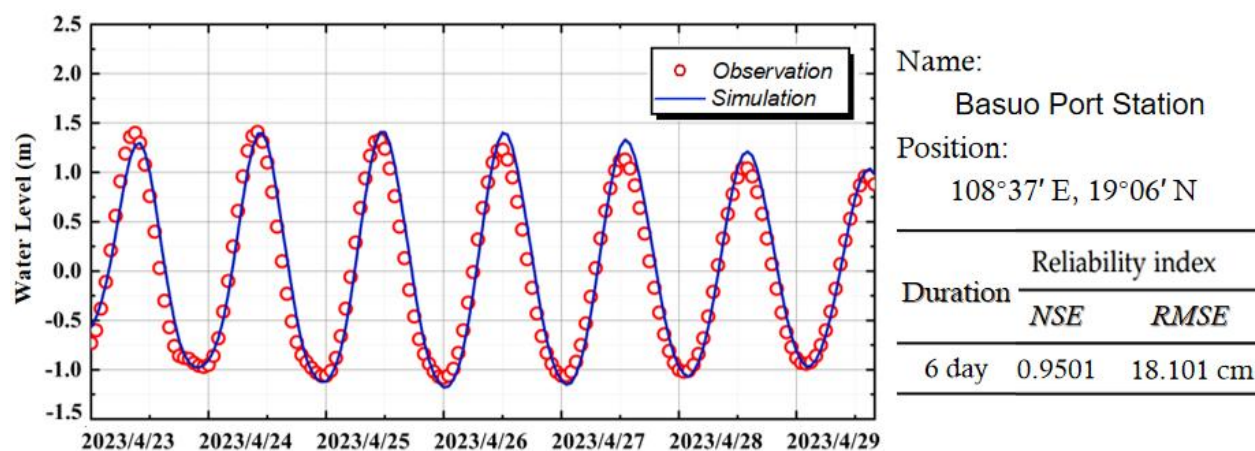
设置格式[Yuxi Wu]: 字体: (中文) Times New Roman, 小三, 英语(美国), (中文)中文(简体)

删除[Yuxi Wu]: 3

删除[Yuxi Wu]: 2

341 108°37'E) and the model simulation results. Model validation occurs from 10:00 on April 23,
 342 2023, to 00:00 on April 30, 2023. After calculation, the RMSE of the simulation results is 18.101
 343 cm and the NSE is 0.9501, which is within the acceptable range. This shows that the model is
 344 reliable and meets the demand, and can be used to simulate the tidal current in the research area
 345 of the lower reaches of Changhua River.

删除[Yuxi Wu]: ,



346

347 **Figure 7** Hourly water level verification of Basuo Port Station

348 During the sea trial, two points were selected to continuously observe the velocity and
 349 direction of seawater. In order to obtain the seawater situation in lunar day, the continuous
 350 measurement time of each point was 25 hours. Information about the position and observation
 351 time of the measuring point is as follows (Table 7 and Figure 8).

352

Table 7 Information of fixed-point current station

Number	Position	Observation
ADCP 01	108°37'28"E, 19°18'10"N	April 23rd at 10: 00 - April 24th at 11: 00
ADCP 02	108°39'21"E, 19°20'55"N	April 24th at 17: 00 - April 25th at 18: 00

设置格式[Yuxi Wu]: 字体颜色: 蓝色

删除[Yuxi Wu]: 5

设置格式[Yuxi Wu]: 字体颜色: 蓝色

删除[Yuxi Wu]: 5

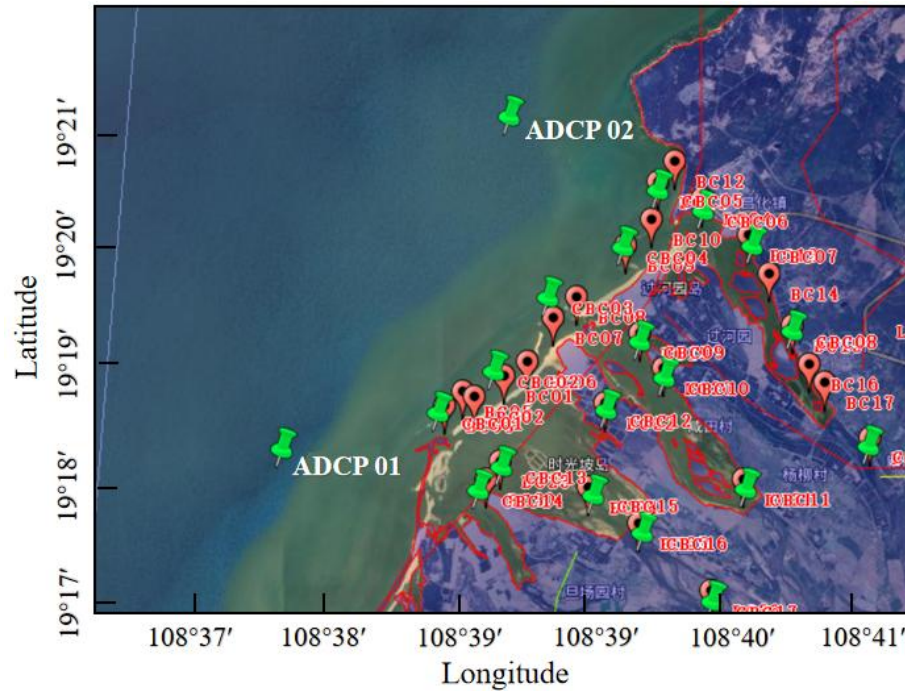
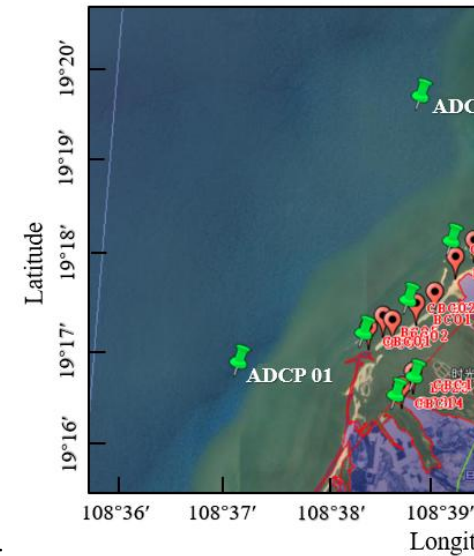


Figure 8 Specific location of ADCP

Current velocity and direction verification at the Changhua River estuary involves a 5-minute time resolution analysis using an Acoustic Doppler Current Profiler (ADCP). Located over 2 km offshore with a water depth of 20.9 m, ADCP 01's data is compared against simulations at five-minute intervals. The 25-hour observation period, from 10:00 on April 23, 2023, to 11:00 on April 24, 2023, encompasses a full lunar day, providing a comprehensive dataset.

The model's simulated velocity and direction are found to be in substantial agreement with the ADCP 01 measurements, particularly in regions where tidal currents are predominant. The model accurately replicates the velocity fluctuations, affirming its capability to capture the dynamics of the study area. The proximity of measurement point ADCP 01 to the land, coupled with its relatively shallow water depth, results in sea water being more susceptible to obstruction by the topography and friction from the seafloor at this location. This results in a reduced error,

设置格式[Yuxi Wu]: 段落间距段前: 6 磅, 段后: 0 磅



删除[Yuxi Wu]:

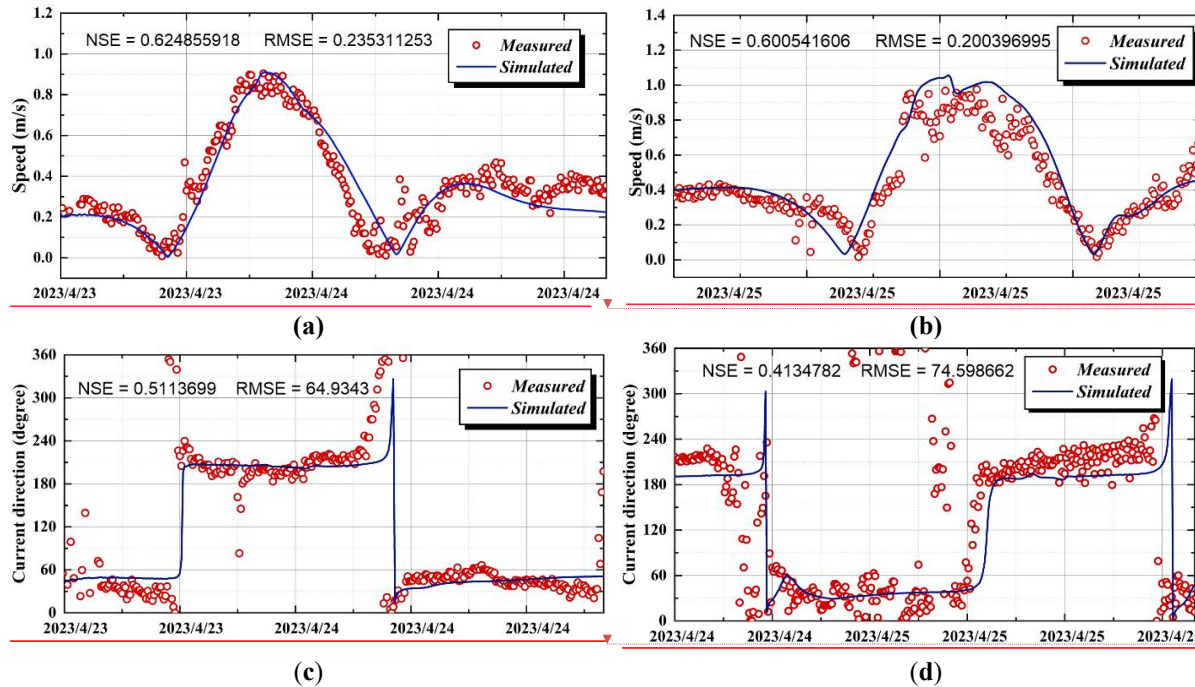
设置格式[Yuxi Wu]: MDPI_5.2_figure, 缩进: 首行缩进: 0 字符, 行距: 单倍行距, 图案: 清除

设置格式[Yuxi Wu]: 字体: (默认) Palatino Linotype, 10 磅, 英语(美国), (中文) 德语(德国)

删除[Yuxi Wu]: 01

删除[Yuxi Wu]: At ADCP 01, the model's predictions are notably accurate due to the shallow water depth and the distance from the shore, which intensify the tidal effects and make the influence of other factors more pronounced.

367 validating the model's performance. The consistency between the model and the measurements
 368 confirms the high reliability of the model for future research applications.



369 **Figure 9** Current velocity and direction verification: (a) velocity verification of ADCP 01; (b) velocity
 370 verification of ADCP 02; (c) verification of current direction of ADCP 01; (d) verification of current
 371 direction of ADCP 02

372 **4.2 Results of hydrodynamic model**

373 The hydrodynamic simulation outcomes, as depicted in [Figure 10](#), indicate a predominantly
 374 NE-SW reciprocating current pattern within the study area. This flow is aligned parallel to the
 375 coastline, with the tidal current shifting direction according to the tidal phase. [Figure 10b and](#)
 376 [10c](#) depict the flow field outside the estuary of the Changhua River. [Figure 10b](#) shows the flow
 377 field at 23:00 on April 23, 2023, corresponding to the peak of the flood tide. At this time, the
 378 tidal current flows in a northeast direction with a maximum speed of 0.62 m/s. [Figure 10c](#) shows
 379 the flow field at 13:30 on April 24, 2023, corresponding to the peak of the ebb tide, where the
 380 tidal current flows in a southwest direction with a maximum speed of 0.75 m/s. Overall, the tidal

删除[Yuxi Wu]:

设置格式[Yuxi Wu]: 段落间距段后: 0 磅

删除[Yuxi Wu]:

设置格式[Yuxi Wu]: 行距: 单倍行距

设置格式[Yuxi Wu]: 段落间距段后: 0 磅

删除[Yuxi Wu]:

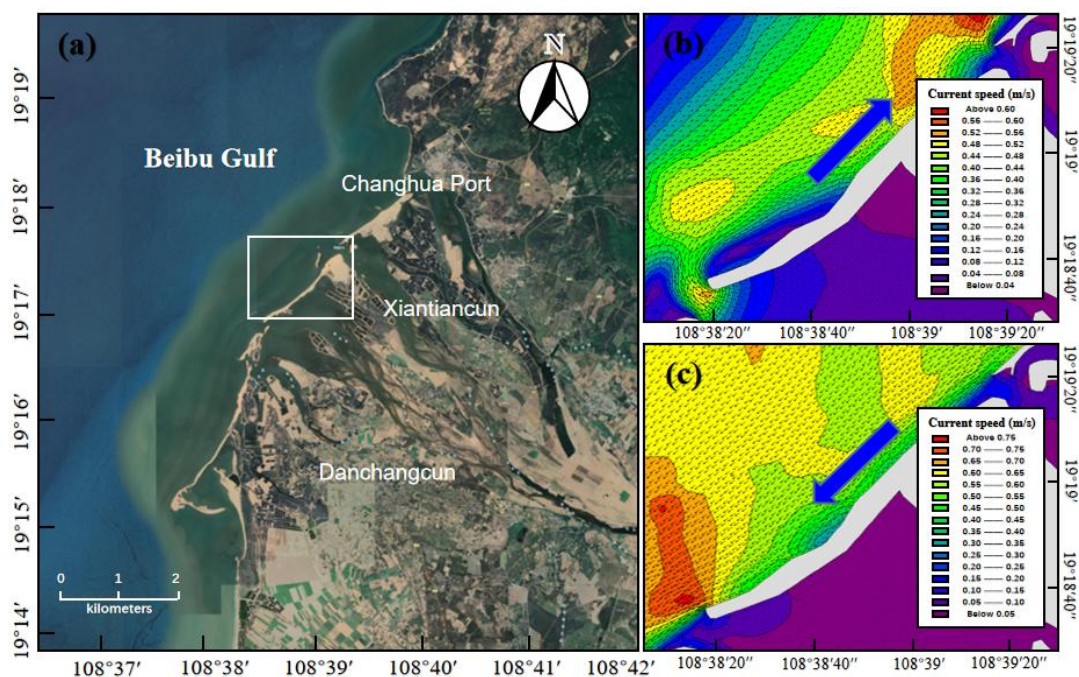
删除[Yuxi Wu]:

删除[Yuxi Wu]: 8

删除[Yuxi Wu]: 3.3

删除[Yuxi Wu]: 9

381 currents outside the Changhua River estuary generally follow a northeast-southwest
 382 reciprocating pattern, with flood tides flowing northeast and ebb tides flowing southwest, parallel
 383 to the shoreline. The maximum ebb current is faster than the maximum flood current.



384
 385 **Figure 10**, Study area and coastal current direction: (a) location map of the study area; (b) detailed zoom of
 386 the map in Fig. 10a with NE current; (c) detailed zoom of the map in Fig. 10a with SW current. (map
 387 origination: <https://hainan.tianditu.gov.cn/>)

388 Figures 11a and 11b illustrate the flow field inside the estuary of the Changhua River.
 389 Figure 11a shows the flow field at 23:00 on April 23, 2023, corresponding to the peak of the
 390 flood tide. Inside Estuary A, due to the topography, a large counterclockwise circulation forms
 391 around the central island, accompanied by several smaller vortices, with the overall trend of tidal
 392 currents flowing southeast along the river channel. In Estuary B, ocean inflows meet with river
 393 flows from upstream, ultimately converging into Estuary C through the passage between B and C.
 394 In Estuary C, the flow is more unidirectional compared to A and B, with upstream water flowing
 395 into the ocean, then following the northeast-directed tidal current outside the Changhua River

删除[Yuxi Wu]: 9

删除[Yuxi Wu]: 9

删除[Yuxi Wu]: 9

设置格式[Yuxi Wu]: 字体: (默认) Times New Roman, ...

设置格式[Yuxi Wu]: 两端对齐, 缩进: 首行缩进: 2 字符 ...

删除[Yuxi Wu]: 0

设置格式[Yuxi Wu]: 字体: (默认) Times New Roman, ...

设置格式[Yuxi Wu]: 字体: (默认) Times New Roman, ...

设置格式[Yuxi Wu]: 字体: (默认) Times New Roman, ...

删除[Yuxi Wu]: 0

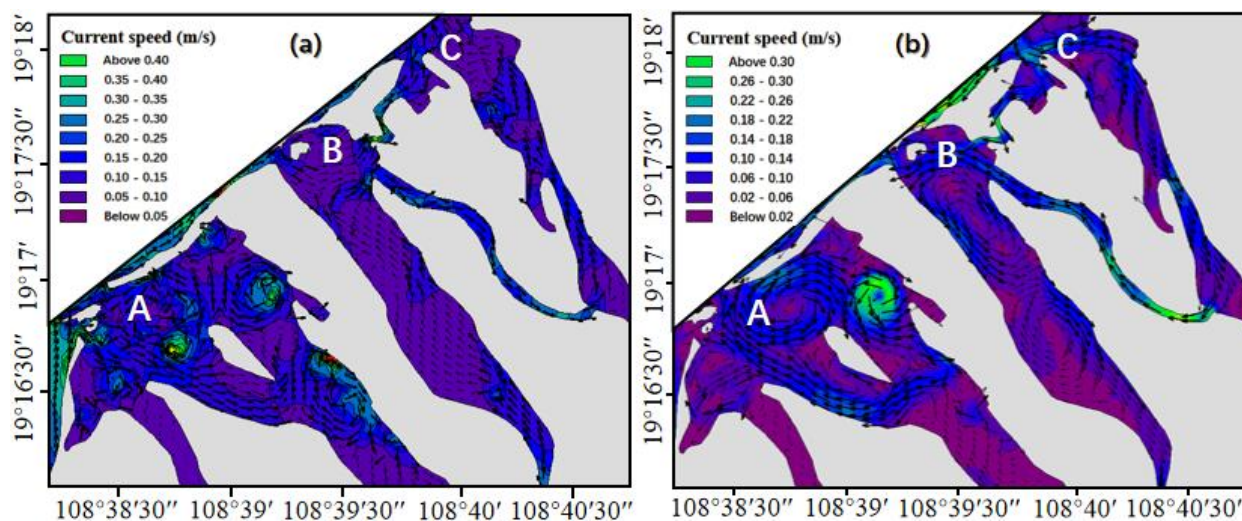
设置格式[Yuxi Wu]: 字体: (默认) Times New Roman, ...

删除[Yuxi Wu]: 0

设置格式[Yuxi Wu]: 字体: (默认) Times New Roman, ...

设置格式[Yuxi Wu]: 字体: (默认) Times New Roman, ...

396 estuary. Figure 11b shows the flow field at 13:30 on April 24, 2023, at the peak of the ebb tide.
 397 At this time, the circulation inside Estuary A reverses to a clockwise direction, and other smaller
 398 vortices change direction accordingly, with the overall trend of tidal currents flowing from
 399 upstream to the ocean. In Estuary B, the dominant force is the high-speed flow from Estuary C,
 400 which enters B through the narrow passage between B and C, splitting into two opposite
 401 directions: one part flows into the ocean, and the other flows upstream, forming a circulation
 402 within the river channel. In Estuary C, the water flows upstream from the ocean along the river
 403 channel.



404 Figure 11. Flow field inside the estuary: (a) moment of the maximum flood current; (b) moment of the
 405 maximum ebb current

407 To further analyze the characteristics of the flow field in the study area, flow fields are
 408 selected for analysis during the transition from low tide to high tide and from high tide to low
 409 tide. Figure 12f depicts the location of the research area. Figure 12a shows the flow field at low
 410 tide, where the tidal current outside the estuary flows northeast, and water in the main river
 411 channel downstream of the Changhua River flows upstream from the ocean. After low tide
 412 (during flood tide), water flow velocity gradually increases, with the tidal current outside the

设置格式[Yuxi Wu]: 字体: (默认) Times New Roman, (中文)等线, 小四, 字体颜色: 蓝色, 字距调整: 1 磅,, (中文)中文(简体), (复杂文种)阿拉伯语(沙特阿拉伯)

删除[Yuxi Wu]: 0

设置格式[Yuxi Wu]: 字体: (默认) Times New Roman, (中文)等线, 小四, 字体颜色: 蓝色, 字距调整: 1 磅,, (中文)中文(简体), (复杂文种)阿拉伯语(沙特阿拉伯)

设置格式[Yuxi Wu]: 字体: (默认) Times New Roman, (中文)等线, 小四, 字体颜色: 自动设置, 字距调整: 1 磅,, (中文)中文(简体), (复杂文种)阿拉伯语(沙特阿拉伯)

设置格式[Yuxi Wu]: 字体: (默认) Times New Roman, (中文)等线, 小四, 字体颜色: 自动设置, 字距调整: 1 磅,, (中文)中文(简体), (复杂文种)阿拉伯语(沙特阿拉伯)

删除[Yuxi Wu]: 0

设置格式[Yuxi Wu]: 字体: (默认) Times New Roman, 小四

设置格式[Yuxi Wu]: 两端对齐, 缩进: 首行缩进: 2 字符, 段落间距段前: 0 磅, 段后: 0 磅, 行距: 固定值 28 磅

设置格式[Yuxi Wu]: 字体: (默认) Times New Roman, 小四

设置格式[Yuxi Wu]: 字体: (默认) Times New Roman, 小四

删除[Yuxi Wu]: 1

设置格式[Yuxi Wu]: 字体: (默认) Times New Roman, 小四

413 estuary consistently flowing northeast. During this period, the main river channel maintains an
414 eastward flow. Figure 12b illustrates the moment of flow direction change during flood tide,
415 when the flow direction outside the estuary rotates clockwise along the shoreline from the south
416 (toward Beili Bay). The northern ocean current (outside Changhua Harbor) also begins to rotate
417 clockwise, flowing into Estuary C, then into the ocean through the passage between B and C,
418 forming a circulation that enhances the clockwise rotation of the northern ocean current.
419 Subsequently, the flow direction gradually changes from northeast to southwest as it moves from
420 the coast toward the open sea. The sand spit at the downstream estuary alters the flow direction
421 and velocity. The sand spit can act as a natural barrier, causing the tidal current to change
422 direction earlier during flood tide. Figure 12c shows the flow field at high tide, where the tidal
423 current outside the estuary has fully shifted to the southwest, while the flow direction further
424 offshore is still transitioning. In the main river channel, the water flows from upstream toward
425 the ocean. Estuaries B and C are influenced by the coastal current outside the northern part of the
426 study area, flowing into the estuary opposite to Estuary A. After high tide (during ebb tide), the
427 water flow velocity in the study area gradually increases, with the tidal current outside the
428 estuary consistently flowing southwest. After some time, the water currents in the southern and
429 northern parts of the study area turn counterclockwise, and the flow direction in the B and C
430 channels changes from inward to outward. Figure 12d shows the flow field at the moment when
431 the flow direction changes during ebb tide. It is evident that there are two counterclockwise
432 circulations outside the Changhua River estuary: one from Beili Bay and the other from outside
433 Changhua Harbor. The latter has a broader influence and thus plays a dominant role in
434 determining the water flow direction in the study area, gradually shifting the coastal current from

删除[Yuxi Wu]: 1

设置格式[Yuxi Wu]: 字体: (默认) Times New Roman, 小四

删除[Yuxi Wu]: 1

设置格式[Yuxi Wu]: 字体: (默认) Times New Roman, 小四

删除[Yuxi Wu]: 1

设置格式[Yuxi Wu]: 字体: (默认) Times New Roman, 小四

435 southwest to northeast. Figure 12e shows the flow field at low tide once again, where the water
436 flow outside the estuary has shifted back to the northeast, repeating the previous flow pattern.

437 In summary, during the transition from flood to ebb tide, the flow field outside the estuary is
438 driven by the deflection of water currents from Beili Bay and Changhua Port, shifting the flow
439 direction from northeast to southwest. During the transition from ebb to flood tide, the deflection
440 is primarily influenced by the circulation outside Changhua Port, shifting the flow direction from
441 southwest to northeast. In channels A, B, and C within the study area, the flow direction changes
442 are relatively consistent due to the passage between B and C. The flow direction in channel A
443 aligns with the main river channel, flowing inward during flood tide and outward toward the
444 ocean during ebb tide.

删除[Yuxi Wu]: 1

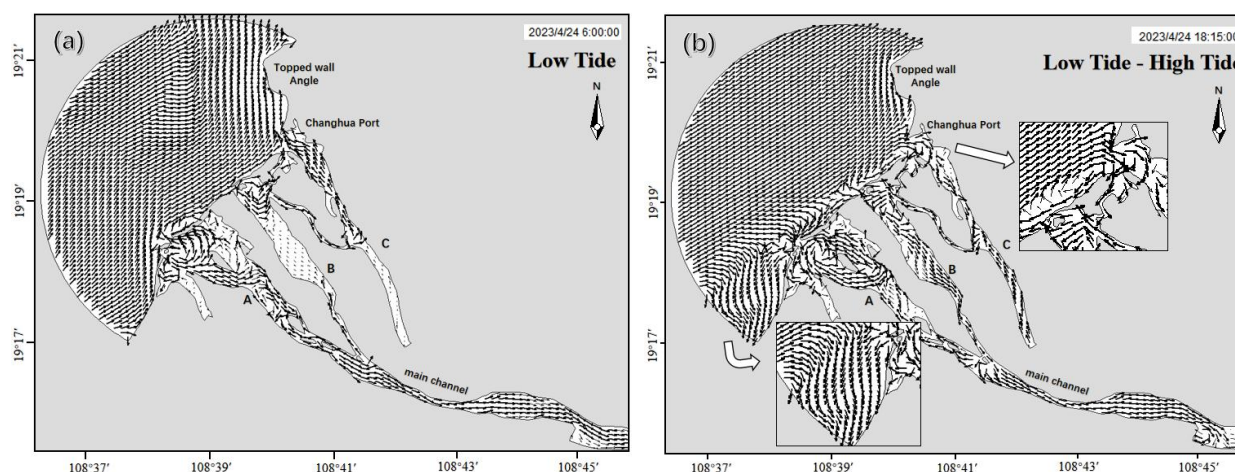
设置格式[Yuxi Wu]: 字体: (默认) Times New Roman, 小四

删除[Yuxi Wu]: Harbor

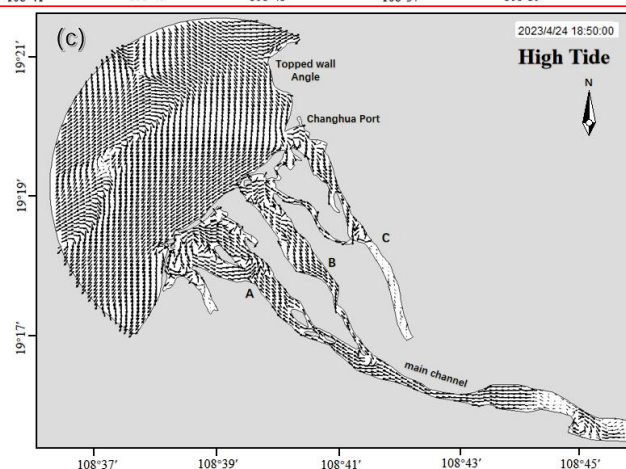
设置格式[Yuxi Wu]: 字体: (默认) Times New Roman, 小四

删除[Yuxi Wu]: Harbor

设置格式[Yuxi Wu]: 字体: (默认) Times New Roman, 小四



445



446

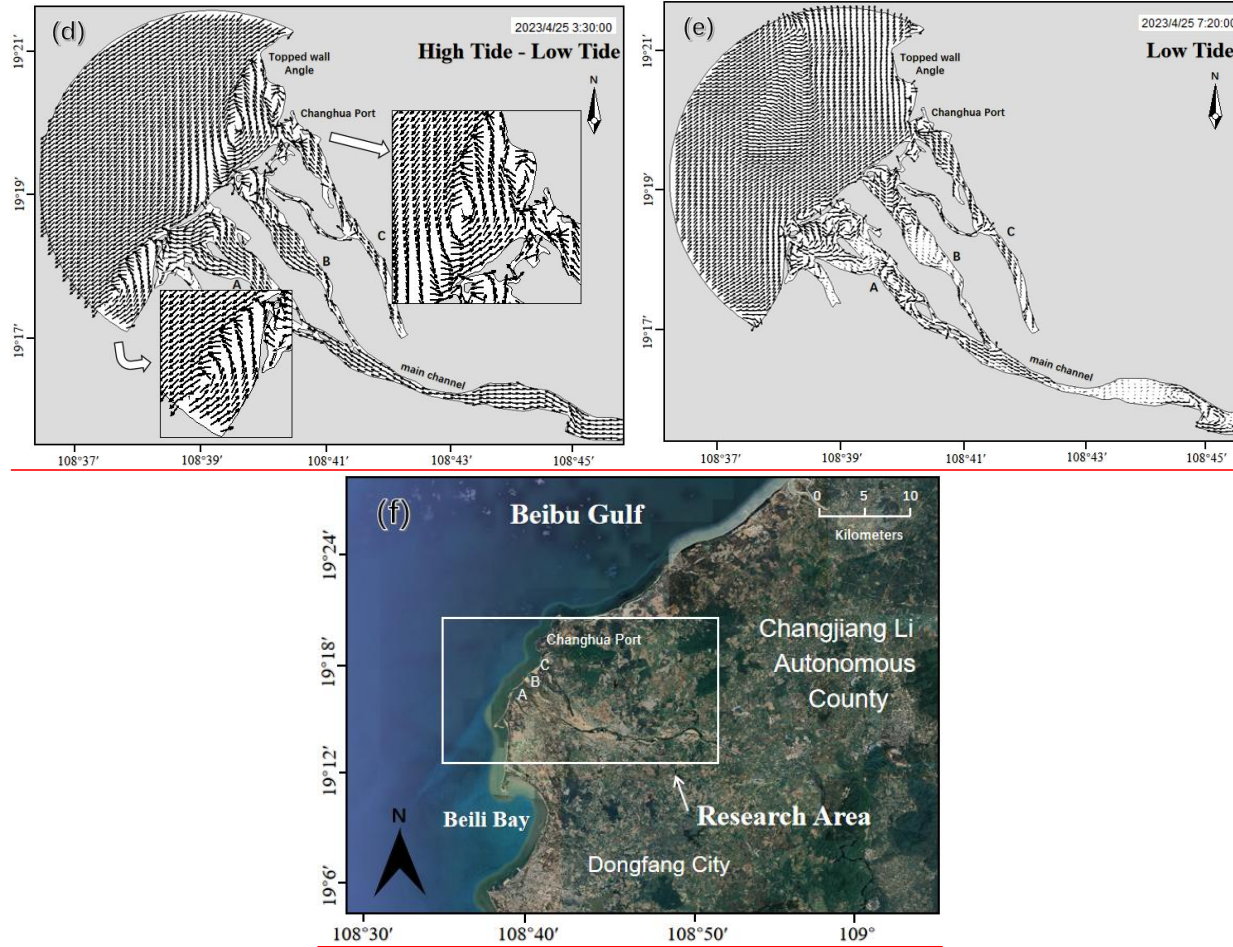


Figure 12 Transition of the flow field (a-e) and location of the study area (f)

5. Sand Transport Model

5.1 Verification by suspended sediment concentration

In the lower reaches of the Changhua River, the summer season is the most pronounced for sediment variation within a year, with the highest sediment concentration and sediment transport rate (Mao et al., 2006). Therefore, sediment data from July, which is representative, are selected for model validation. The simulated Suspended Sediment Concentration (SSC) is compared with

删除[Yuxi Wu]: 5. Sand Transport Model

设置格式[Yuxi Wu]: Heading-Main, 段落间距段前: 24 磅, 行距: 2 倍行距

设置格式[Yuxi Wu]: 字体: (中文) Times New Roman

删除[Yuxi Wu]: 3.4

删除[Yuxi Wu]: of sediment model

删除[Yuxi Wu]: To validate the effectiveness of the sediment model, a combination of theoretical and empirical validation methods is employed to verify the simulation results. Theoretical validation is conducted using the sediment transport rate method to calculate the annual sediment

457 the daily observed SSC at Baoqiao Station for the month of July (Figure 13). The SSC at
458 Baoqiao Station is the highest during the first two days of July, reaching a peak SSC of 0.55
459 kg/m³. Subsequently, the SSC continuously decreases, reaching its lowest value on the 5th of
460 July, and then slowly rises. After the 10th of July, it gradually decreases from 0.301 kg/m³, with
461 the most values remaining below 0.2 kg/m³. Based on the analysis, NSE for Baoqiao Station is
462 0.8389; the RMSE is 0.097244 kg/m³. The observed SSC are in good agreement with the
463 simulated values.

464 To further analyze the simulation validation, Figure 13 presents a histogram of the daily
465 absolute error in SSC at Baoqiao Station. The absolute error is calculated as the absolute
466 difference between the measured and simulated values. The Mean Absolute Error (MAE) is
467 defined as the average over the test sample of the absolute differences between prediction and
468 actual observation. The MAE in SSC for Baoqiao Station in July is 0.071224 kg/m³. The
469 maximum error occurs at the beginning and the end of the month, which may be due to the use of
470 monthly average flow and sediment data for the model's upper boundary input, thereby
471 increasing the model's error. Overall, the difference between the daily observed SSC values and
472 the simulated results at Baoqiao Station in July is within a reasonable range, indicating that the
473 model has an acceptable level of precision.

删除[Yuxi Wu]: 2

删除[Yuxi Wu]: 2

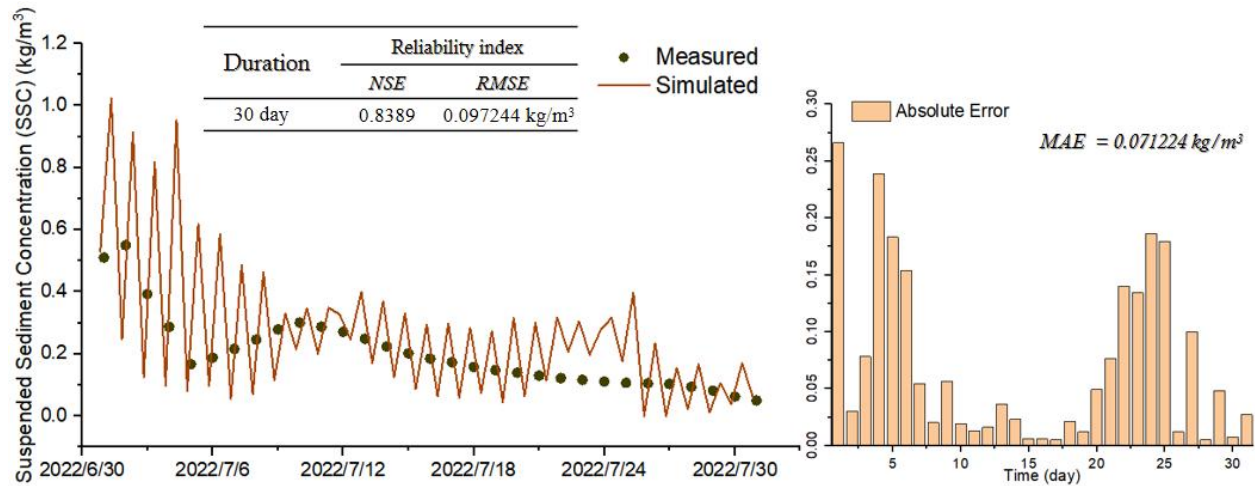


Figure 13 Selection point for sediment deposition verification

删除[Yuxi Wu]: 2

5.2 Analysis of depositions in Changhua River estuary

删除[Yuxi Wu]: 3.5

Sediment deposition in the Changhua River estuary is influenced by both hydrodynamic and geological factors. The predominant northeast-southwest tidal current direction and wave action, has led to the formation of a two-way sand mouth, further narrowing the estuary. Secondly, the estuary's geomorphology consists of a sandy riverbed with poor stability. The bed slope at the estuary decreases, and the water flow's capacity to carry sediment is reduced. Therefore, the sediment accumulation at the mouth of the Changhua River is relatively severe..

删除[Yuxi Wu]: coastal

Over time, these processes have resulted in the formation of two river islands, altering the estuary into a complex channel system with multiple smaller estuaries. Currently, the main river channel flows between these islands, exhibiting shallow depths during low tide. These findings are pivotal for understanding the estuary's morphological evolution and inform strategies for sediment management in such dynamic environments.

There are two obvious depositions in the study area, including the estuary and the slender channel. The figure clearly shows the serious and slight areas of siltation in the study area. However, the specific sedimentary characteristic in the study area is unknown, needing further

删除[Yuxi Wu]: The result of the sediment simulation (Figure 10) shows the variation of sediment thickness in the study area after one week of simulation.

491 analysis. To solve this problem, we extract the bed level change data of a point in the obvious
492 change area of river bed, and take this point as the whole area. Therefore, the sediment
493 deposition characteristic in this area can be analyzed through the bed level change at this point.



设置格式[Yuxi Wu]: MDPI_5.2_figure

494

495 Figure 14: Information of important place names in simulated areas

496 Results of Danchangcun are shown in Figure 15, which illustrates the bed level changes and
497 consequent sediment deposition and scouring in various parts of Danchangcun. Positive values
498 indicate sediment deposition, while negative values denote scouring.

删除[Yuxi Wu]: 43

499 In the estuary of Danchangcun (Figure 15b), the bed level fluctuates above zero, signifying
500 net sediment deposition with a final accumulation of approximately 0.59 cm over the simulation
501 period.

删除[Yuxi Wu]: 43

502 The deposition near the river island in Danchangcun (Figure 15d) follows a cyclical pattern
503 over a 24-hour cycle, with an overall sediment thickness of about 0.20 cm. Initially, sediment
504 accumulates quickly, after which the bed level stabilizes at its peak value. A sharp decrease in
505 deposition rate is observed in the last two hours, with each cycle adding about 0.03 cm of

删除[Yuxi Wu]: 43

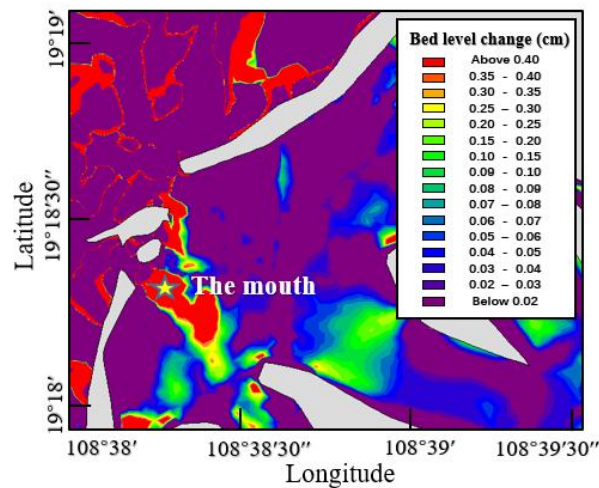
506 sediment.

507 At the front end of the sand mouth (Figure 15f), the bed level decreases by 0.39 cm,
508 indicating active scouring and sediment removal. The continuous negative bed level changes
509 suggest an increasing scouring intensity, especially pronounced on April 23 when a significant
510 erosion event led to a 0.18 cm drop in bed level.

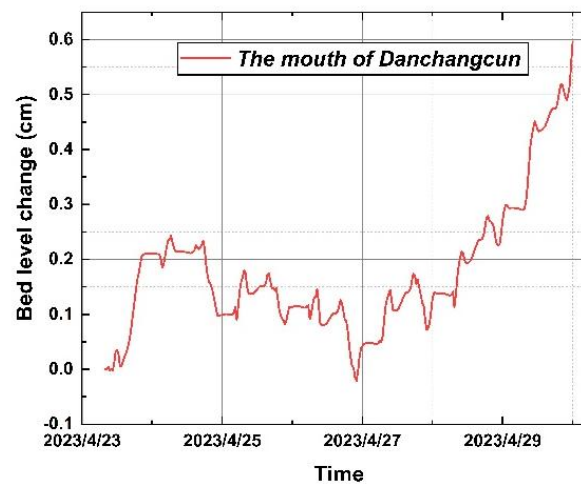
511 Finally, Figure 15h examines sediment deposition at the sand mouth, with two distinct
512 locations showing similar sedimentation trends, albeit with Location 2 (near the river)
513 experiencing faster sedimentation. Prior to April 24-25, Location 1 (near the ocean) registered
514 erosion, followed by a transition to net deposition, while Location 2 showed minor erosion
515 before April 24. The simulation predicts final bed level changes of approximately 0.42 cm for
516 Location 1 and 0.60 cm for Location 2.

删除[Yuxi Wu]: 43

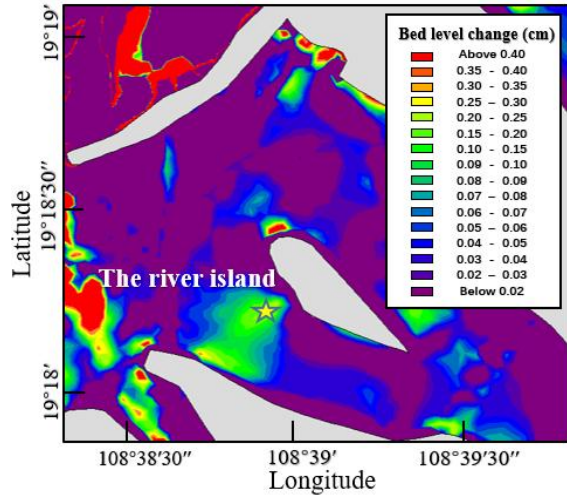
删除[Yuxi Wu]: 43



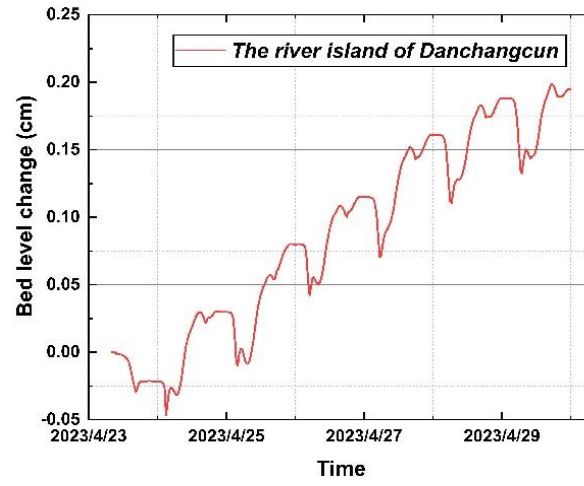
(a)



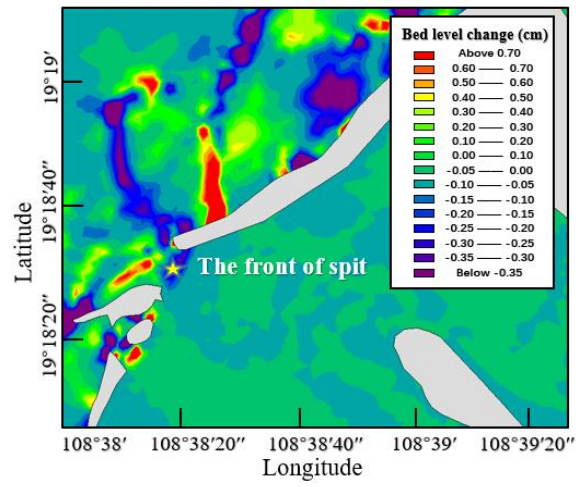
(b)



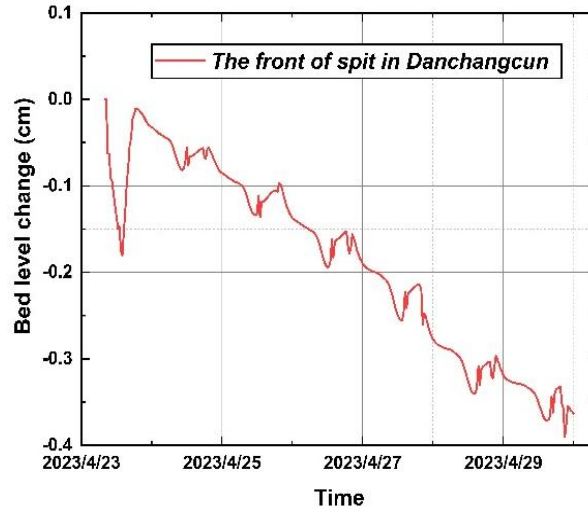
(c)



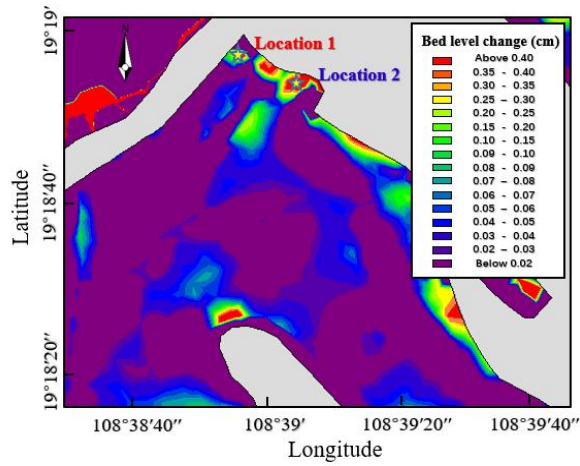
(d)



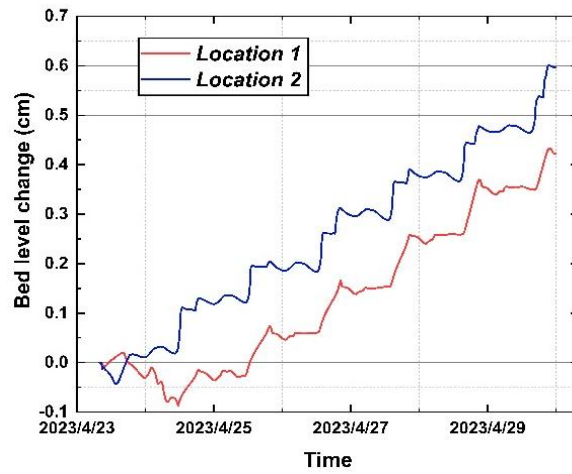
(e)



(f)



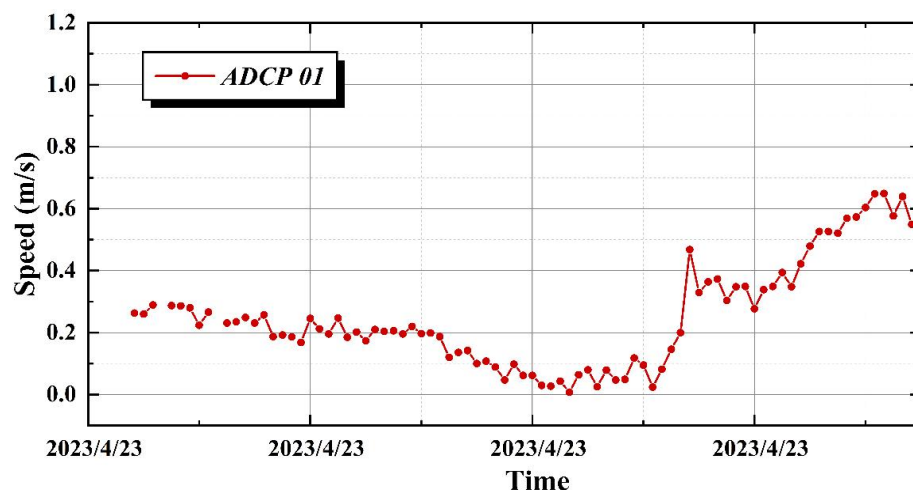
(g)



(h)

518 From April 27th to 30th, an overall increase in deposition thickness was noted, reaching
519 approximately 0.59 cm. Two rapid deposition phases were identified: the first, on April 23rd
520 from 13:30 to 20:30, coincided with astronomical mid-tide but exhibited lower current velocities
521 than expected, as per ADCP 01 measurements. The second phase followed an spring tide on
522 April 22nd, which stirred turbulent currents and enhanced scouring, leading to increased
523 sediment concentration in the estuary. The tide on April 23rd was moderate, significantly
524 reducing current velocity and sediment transport capacity, resulting in sediment deposition in the
525 estuary.

526 On April 27th, during astronomical neap tide, lower water levels and reduced tidal ranges
527 led to slower currents, enhancing sedimentation and weakening lateral erosion. The current's
528 reduced capacity limited the transport of larger sediment particles, allowing only fine grains to
529 settle at the water's bottom. These findings underscore the complex interplay between sediment
530 deposition and erosion in estuarine environments and highlight the influence of tidal dynamics
531 on sediment transport processes.



532

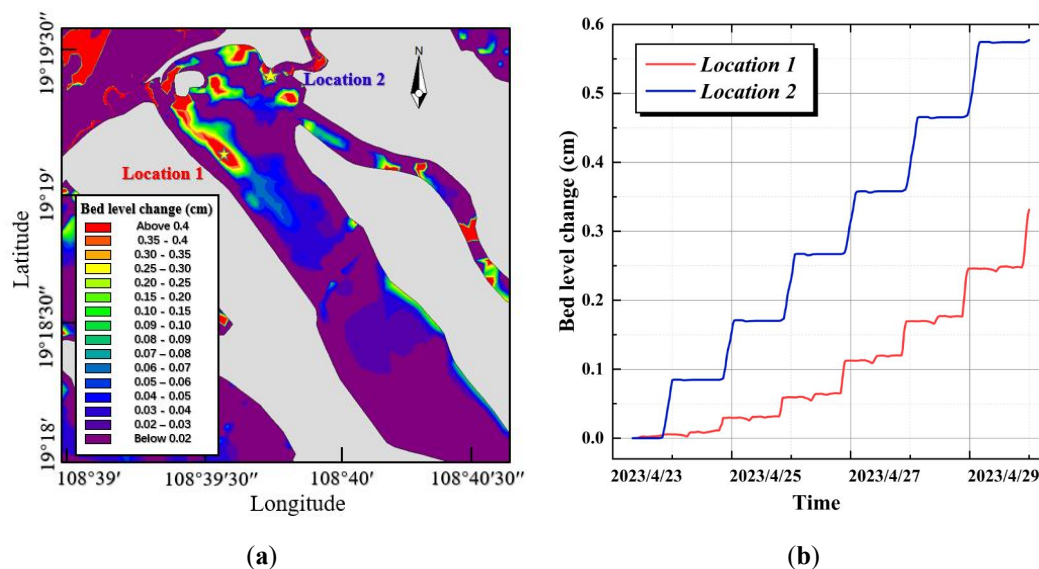
533 Figure 16 Current speed on April 23rd

删除[Yuxi Wu]: 54

534 In the Xiantiancun estuary, sediment deposition is influenced by its narrower configuration

535 compared to Danchangcun, with numerous tributaries contributing to a dispersed flow and
 536 reduced kinetic energy. This results in variable sediment deposition levels at the entrances of the
 537 tributaries, although the overall deposition is less extensive than at the Danchangcun mouth. The
 538 maximum observed deposition thickness within the estuary is 0.58 cm at Location 2, while other
 539 areas exhibit thicknesses between 0.3 cm and 0.5 cm.

540 Two significant deposition sites are located near the sand mouth, which may facilitate the
 541 mouth's further expansion. Additionally, a substantial, albeit thin, silting zone is identified at the
 542 rear of the river island (Location 1), covering a considerable area. These findings indicate the
 543 complex interplay of sedimentary processes in estuarine environments and the potential for
 544 morphological changes due to deposition patterns.



545 **Figure 17.** Deposition in Xiantiancun: (a) shows changes of sedimentation thickness of Xiantiancun with
 546 palette; (b) shows changes of sedimentation thickness of Xiantiancun in detail.

删除[Yuxi Wu]: 65

547 To summarise, the Changhua River estuary exhibits distinct sedimentation patterns, with
 548 notable deposition occurring in both the estuary and slender channel regions. The estuary
 549 depositions are a result of interplay between hydrodynamic conditions and geological settings.
 550 Specifically, the estuary is subject to persistent northeast-southwest coastal currents and wave

551 action, leading to the formation of a two-way sand mouth that constricts the estuary's width. The
552 sandy, unstable riverbed further contributes to substantial sediment deposition due to the reduced
553 gradient and sediment transport capacity of the fluctuating discharge. This has, over time, led to
554 the formation of river islands, transforming the estuary into a complex channel system with
555 multiple small estuaries. The main channel, situated between these islands, experiences shallow
556 water depths during low tide.

557 In the Danchangcun region, the estuary displays a maximum sediment deposition thickness
558 of 0.59 cm. The presence of a small river island in this area results in shallow deposition near the
559 island, with some areas having thicknesses below 0.3 cm. In contrast, deeper deposition is
560 observed along the riverbanks and particularly near the estuary. The sand mouth at the estuary's
561 entrance is influenced by river erosion and coastal currents, leading to the formation of a new
562 small sand mouth to the southwest. The original sand mouth tends to thicken after fracturing,
563 with scouring at its front end and deposition at the fractured end, reaching a maximum thickness
564 of 0.6 cm. This suggests that the estuary's current is obstructed by multiple depositional strips,
565 resulting in a slower current and increased deposition.

566 In the Xiantiancun region, the estuary is narrower than in Danchangcun, with numerous
567 tributaries dispersing the flow and reducing energy. This leads to varying degrees of deposition at
568 the entrances of the tributaries, although the overall deposition is less than that observed at the
569 Danchangcun mouth. The maximum deposition thickness at the estuary reaches 0.58 cm, with
570 other areas exhibiting thicknesses ranging from 0.3 cm to 0.5 cm. Deposition near the sand
571 mouth contributes to its expansion, and a long silting zone is present at the rear of the river island,
572 characterized by a thin layer over a large area.

573 **5.3 Analysis of deposition in Changhua River channel**

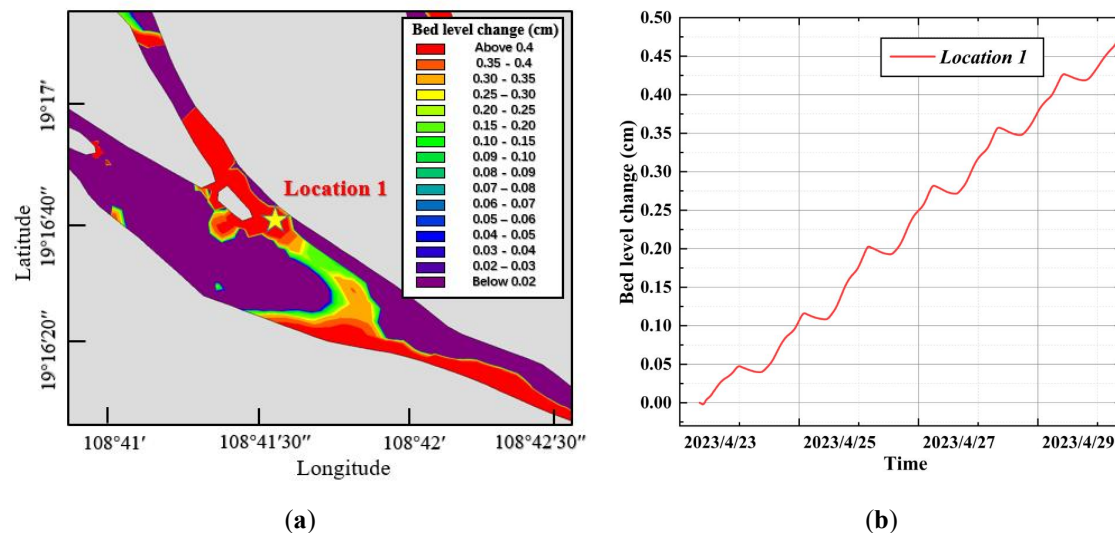
删除[Yuxi Wu]: 3.6

574 Changhua River's channel exhibits two key sediment deposition sites: the Chahe confluence
575 and an area near Jiuxiancun. These areas are prone to significant sedimentation as the river
576 narrows from a wide estuary to a more confined channel, increasing the risk of blockages(Figure
577 18a). The primary sedimentation zone is located on the right bank of the distributary, with the
578 maximum thickness measuring 0.47 cm (Figure 18b). Deposition is most intense around the river
579 island and decreases from the right side towards the rear and the left side of the island. This
580 distribution suggests that sedimentation is more pronounced in the upper, narrower section of the
581 channel.

删除[Yuxi Wu]: 76

删除[Yuxi Wu]: 76

582 In the main channel, erosion occurs on the ocean-facing right side, while the left side is
583 subject to deposition. The sediments on the left bank are likely sourced from tidal actions or
584 upstream inflows, a process that requires further study. The lateral variation in sedimentation and
585 scouring highlights the intricate sediment dynamics within the river channel.



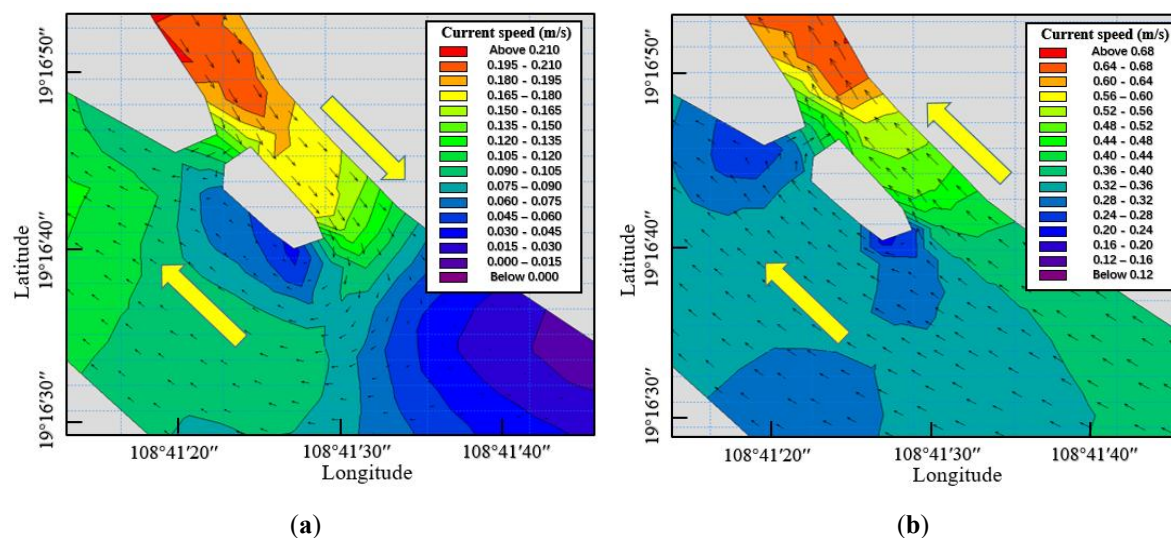
586 **Figure 18**, Deposition in channel: (a) shows changes of sedimentation thickness of channel with palette; (b)
587 shows changes of sedimentation thickness of channel in detail.

删除[Yuxi Wu]: 76

588 Analysis of topography and flow velocities along the river island banks indicates a pattern

589 of alternating unidirectional and counter-currents (Figure 19). The current speeds peak at 0.21
 590 m/s during opposing flows and reach approximately 0.68 m/s when currents are in the same
 591 direction. The Xiantiancun section, marked by a constricted channel and intensified currents, is
 592 prone to sediment accumulation. As tides recede, the river's hydrodynamic energy weakens,
 593 facilitating the convergence of the Xiantiancun course with the estuary's incoming flows. This
 594 interaction leads to the predominant deposition of sediment on the left bank of the main channel,
 595 facing the ocean, which is influenced by high-tide influxes.

删除[Yuxi Wu]: 87

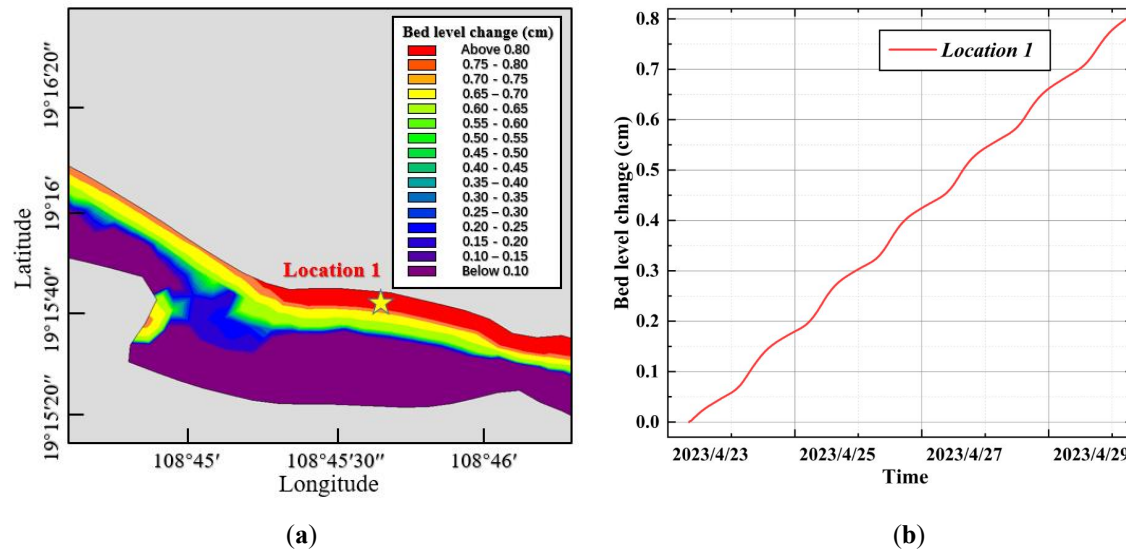


596 Figure 19 Flow around the river island: (a) shows the flow around river island in opposite directions; (b)
 597 shows the flow around river island in same directions

删除[Yuxi Wu]: 87

598 A secondary sediment deposition site has been identified in proximity to Jiuxiancun, with
 599 the maximal sediment thickness measuring 0.81 cm (Figure 20). This deposition zone is
 600 elongated and in close proximity to the coast, while erosion is observed on the opposing bank.
 601 The river's erosive action has led to the removal of the opposite bank, with the displaced
 602 sediment accumulating near Jiuxiancun. Over time, this accumulation is expected to enhance the
 603 river bend's curvature, potentially hindering the river's natural evolution.

删除[Yuxi Wu]: 198



604 **Figure 20** Deposition near the Jiuxiancun: (a) shows changes of sedimentation thickness of Jiuxiancun
 605 with palette; (b) shows changes of sedimentation thickness of Jiuxiancun in detail.

删除[Yuxi Wu]: 198

606 To summarise, there are two clear deposits at the channel of the Changhua River. One occurs
 607 at the intersection of Xiantiancun and Danchangcun, while the other is near Jiuxiancun.
 608 Compared to the fork, sedimentation near the Jiuxiancun is deeper and thicker. The final
 609 deposition thickness of the model is 0.81 cm. The fork was deposited near the river island, and
 610 the simulation resulted in a displacement of 0.47 cm. The sediment carried by the high tide may
 611 be the source.

6. Discussion

6.1 Residual Current

614 Residual currents to some extent reflect the transfer and exchange of water bodies, and their
 615 direction is usually the direction of sediment movement and the dispersion and migration of
 616 pollutant substances (Robinson, 1983). They are closely related to the long-term transfer and
 617 deposition of estuarine materials. Therefore, studying the characteristics of residual currents in

删除[Yuxi Wu]:

64. Causes of sediment depositionDiscussion

设置格式[Yuxi Wu]: 正文, 缩进: 首行缩进: 2 字符, 段落
 间距段前: 0 磅, 行距: 固定值 28 磅, 图案: 清除(白色)

删除[Yuxi Wu]: Measurements for sediment regulation

设置格式[Yuxi Wu]: 字体: (中文) Times New Roman

删除[Yuxi Wu]: 4

删除[Yuxi Wu]: Influence of r

删除[Yuxi Wu]: c

删除[Yuxi Wu]: in low water periodAnticipated
 Regulation Measures for Estuary Siltation

设置格式[Yuxi Wu]: 字体颜色: 蓝色

618 this sea area under the combined action of waves and currents can comprehensively understand
619 the evolution characteristics of the sea area's sediment. Tidal residual currents can be studied
620 using the Lagrangian and Eulerian methods. Eulerian residual current refers to the average
621 transfer caused by the average flow after removing the periodic astronomical tide, and its
622 magnitude and direction mainly depend on the strength and duration of the ebb and flood tidal
623 velocities within the tidal cycle; Stokes' drift characterizes the net drift of the water body, and its
624 numerical size directly reflects the correlation between the tidal range and the change in flow
625 velocity within the tidal cycle, and the sum of the two is the Lagrangian residual current. The
626 Lagrangian residual current is not the result of the long-term tracking of real particles, but is the
627 result of the superposition of Eulerian residual current and Stokes' drift.

628 Eulerian residual current refers to the average transfer caused by the average flow after
629 removing the periodic astronomical tide, and its magnitude and direction mainly depend on the
630 strength and duration of the ebb and flood tidal velocities within the tidal cycle; Stokes' drift
631 characterizes the net drift of the water body, and its numerical size directly reflects the
632 correlation between the tidal range and the change in flow velocity within the tidal cycle, and the
633 sum of the two is the Lagrangian residual current. The formulas for calculating Eulerian residual
634 current and Stokes' drift refer to previous studies (Longuet-Higgins, 1969; Uncles and Jordan,
635 1980; Li and O'Donnell, 1997).

636 Through the analysis of sediment simulation results from the previous section on the
637 distribution of major sedimentation areas, we have been able to understand the distribution of
638 these areas. However, the causes of sedimentation require further exploration. In this section,
639 based on the tidal current field data from hydrodynamic numerical simulation, we calculate the
640 residual flow according to the entire study area. The flow velocity measured data from two

641 ADCP stations outside the estuary of the Changhua River was analyzed using the tidal residual
642 current calculation method, thereby enhancing the credibility of the residual flow field.

643 Table 8 Residual currents in spring neap tide at each station

<u>Station</u>	<u>Eulerian residual current</u>		<u>Stokes' drift</u>		<u>Lagrangian residual current</u>	
	<u>Speed (m/s)</u>	<u>Degree (°)</u>	<u>Speed (m/s)</u>	<u>Degree (°)</u>	<u>Speed (m/s)</u>	<u>Degree (°)</u>
<u>ADCP01</u>	<u>0.0913</u>	<u>232</u>	<u>0.0006</u>	<u>172</u>	<u>0.0917</u>	<u>231</u>
<u>ADCP02</u>	<u>0.0331</u>	<u>137</u>	<u>0.0007</u>	<u>194</u>	<u>0.0335</u>	<u>138</u>

644 The Lagrangian residual current at monitoring station ADCP01 is 0.0913 m/s with a
645 direction of 231° (SW), and at station ADCP02 it is 0.0331 m/s with a direction of 138° (NW)
646 (Table 8). In the area outside the Changhua River estuary, the Stokes tidal residual current at the
647 monitoring stations is two orders of magnitude smaller than the Eulerian residual current.
648 Therefore, the flow trend of the composite Lagrangian tidal residual current remains essentially
649 consistent with that of the Eulerian residual current.

650 6.2 Influence of residual current in low water period

651 The study area has a distinct monsoon climate, with prevailing southerly winds in the
652 summer and alternating southerly and northeasterly winds in the spring. The figure 20 shows the
653 Eulerian residual current field during the simulation period (low water period). To present the
654 Eulerian residual currents within the study area in a complete and clear manner, a limit on vector
655 length was set when plotting the current field. Consequently, the direction and length of the
656 arrows in the figure represent the direction of the residual currents, but not their intensity.
657 However, the intensity of the Eulerian residual currents can still be discerned through the data at
658 the grid points. The Eulerian residual current outside the Changhua River estuary generally flows
659 southward. As it flows from north to south, it is obstructed by the sand spit, diverging around it.

设置格式[Yuxi Wu]: 字体: (中文)等线, 五号, 字体颜色: 蓝色

设置格式[Yuxi Wu]: MDPI_5.2_figure, 缩进: 首行缩进: 0 字符, 行距: 单倍行距, 图案: 清除

设置格式[Yuxi Wu]: 字体: (中文)等线, 五号

设置格式[Yuxi Wu]: 字体颜色: 蓝色

删除[Yuxi Wu]: According to the previous analysis, the Changhua River estuary is controlled by tides, and there is a long-term repeated coastal flow. Therefore, the current drives the sediment in the river bed to form a composite channel. According to the results of the sediment transport model, the main sediment deposition near the estuary occurs in Danchangyuan Village and Xiantian Village. Based on the formation mechanism of estuarine sediment, the following two measures are put forward.

设置格式[Yuxi Wu]: Heading-Secondary, 缩进: 左侧: 3.7 毫米, 首行缩进: 0 字符, 右侧: 3.7 毫米, 段落间距段前: 18 磅, 行距: 1.5 倍行距, 图案: 清除, 2 级

设置格式[Yuxi Wu]: 字体: 四号

设置格式[Yuxi Wu]: 字体颜色: 蓝色

660 After the divergence, the southwestward Eulerian residual current splits, with one part following
661 the sand spit to the river mouth near A, and the other part entering channel B and flowing inward.
662 The northeastward Eulerian residual current, after divergence, encounters the obstruction of the
663 headland (Topped wall Angle) and forms a counterclockwise circulation below Junbi Jiao.
664 Headlands are one of the key topographical features where strong residual current vortices occur
665 (Maddock et al., 1978; Pingree et al., 1977; Smith, 2010). At the headland, the water depth
666 shoals in the onshore direction, and the frictional effect is stronger in shallow water areas than in
667 deep water areas. This results in a frictional force moment on the alongshore tidal current,
668 generating vorticity. The transport of vorticity within the closed circulation lines on either side of
669 the headland is not equal in input and output. After a tidal cycle of time averaging, a net vorticity
670 will be produced on both sides of the headland, forming two counter-rotating residual current
671 vortices, with the tidal residual current at the tip of the headland generally pointing seaward
672 (Zimmerman, 1981). Topped wall Angle, being a headland, can produce similar residual current
673 field results. A clockwise residual current vortex opposite to the one below may exist above
674 Topped wall Angle. The Eulerian residual currents in the three river channels where A, B, and C
675 are located all flow towards the river mouths. The Eulerian residual current in the channel
676 between B and C flows from B to C.

设置格式[Yuxi Wu]: 字体颜色: 蓝色

设置格式[Yuxi Wu]: 字体颜色: 蓝色

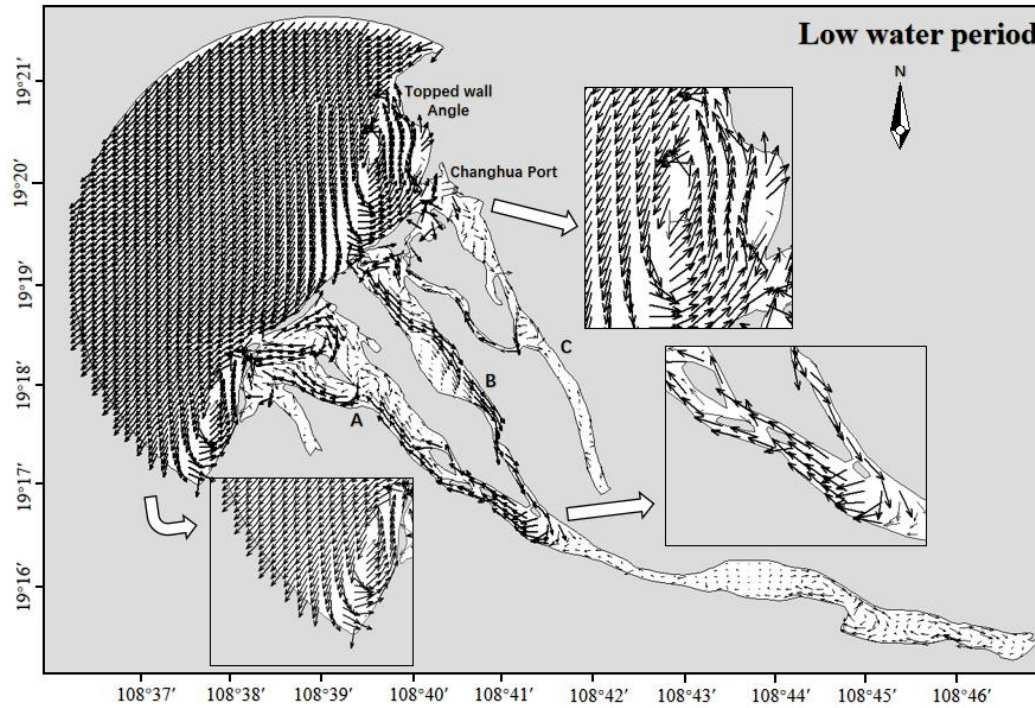


Figure 21 Eulerian residual current field during low water period

6.3 Influence of residual current in high water period

In order to comprehensively understand the residual current field of the study area, it is essential to analyze the residual current field during the flood season. The figure displays the Eulerian residual current field of the study area for July 2022 (high water period). The Eulerian residual current south of the river mouth in the study area still flows to the south (towards Beili Bay), but the nearshore residual current veers more quickly, resulting in a smaller circulation compared to the dry season. The circulation range in the north has expanded, likely due to the influence of the southerly monsoon during the summer, leading to an increase in the strength and directional deflection of the Eulerian residual current. When it reaches the shore, it is naturally obstructed by the sand spit and disperses to both sides (NE-SW). The upward Eulerian residual current, upon encountering the sea area outside Changhua Port, is deflected by the coastal

设置格式[Yuxi Wu]: MDPI_5.2_figure, 缩进: 首行缩进: 0 字符, 行距: 单倍行距, 图案: 清除

删除[Yuxi Wu]: 1

删除[Yuxi Wu]: 09

删除[Yuxi Wu]: Deposition near the Jiuxiancun: (a) shows changes of sedimentation thickness of Jiuxiancun with palette; (b) shows changes of sedimentation thickness of Jiuxiancun in detail.

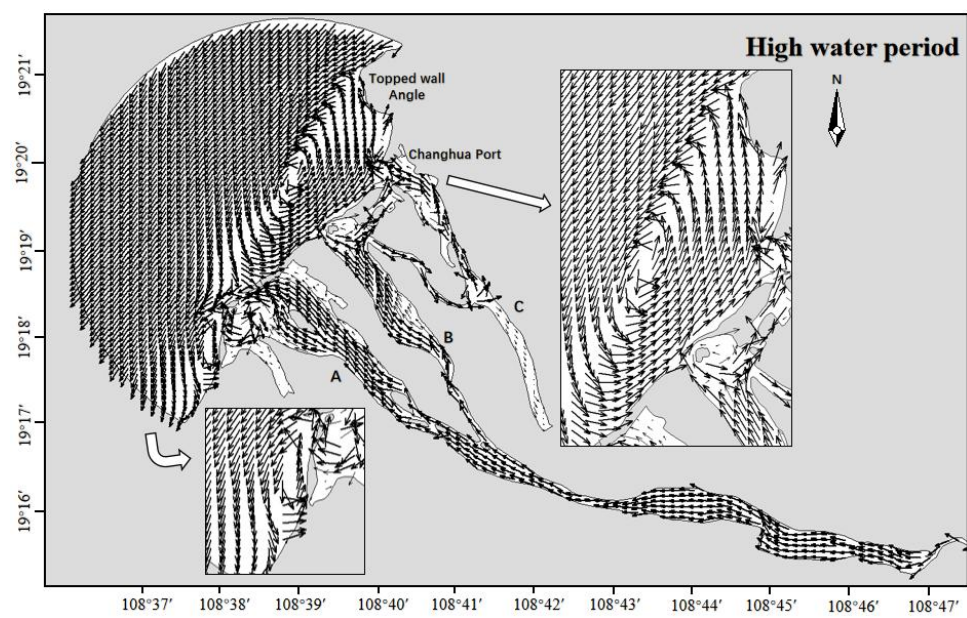
设置格式[Yuxi Wu]: 字体: (中文) 等线

设置格式[Yuxi Wu]: MDPI_5.2_figure, 缩进: 首行缩进: 0 字符, 行距: 单倍行距, 图案: 清除

删除[Yuxi Wu]: The slope protection of dikes within tidal estuaries necessitates an engineering approach that prioritizes resilience against environmental impacts, structural integrity, and effective wave dissipation. Additionally, these measures should exhibit longevity and ease of construction, mainten

删除[Yuxi Wu]: An objective analysis of sediment content in the river channel is needed to further assess the situation. The tables below provide statistics for the annual average sediment transport and sediment concentration at the Baoqiao station in the lower reaches of Changhua River.

691 promontory (Topped wall Angle) and turns westward. The westward Eulerian residual current,
692 continuously affected by the strong southerly winds during its movement, keeps deflecting.
693 Eventually, a circulation is formed, with a circulation range larger than that of the dry season.
694 The situation in channel A is essentially consistent with the dry season, while the Eulerian
695 residual current directions in channel B and C are the same as that in A, all flowing towards the
696 ocean. This is quite different from the dry season, with a flow direction opposite to that of the
697 dry season, which may be related to the increased rainfall and subsequent increase in
698 downstream flow during the summer flood season.



699
700 Figure 22 Eulerian residual current field during high water period

701 **7. Conclusions**

702 The study successfully applied a wave-current coupled sediment transport model to the
703 lower reaches of the Changhua River in Hainan Island. By integrating field measurements,
704 remote sensing techniques, and the Van Rijn model, this research has developed a comprehensive

设置格式[Yuxi Wu]: MDPI_5.2_figure, 缩进: 首行缩进: 0
字符, 行距: 单倍行距, 图案: 清除

设置格式[Yuxi Wu]: 段落间距段前: 12 磅

删除[Yuxi Wu]: 1

删除[Yuxi Wu]: Scheme 3: Recognizing the distinct flood
(May-October) and dry (November-April) seasons of the
Changhua River, with the flood season accounting for 77% of
the annual flow, it is proposed to establish seasonal gates
within the river. These gates can control the flow by adjusting
the number and operation mode of inlets and outlets.
Additionally, grab dredgers can be utilized to assist in river
dredging during the flood season.

删除[Yuxi Wu]: 5

705 model capable of accurately simulating sediment behavior under the combined action of waves
706 and currents. The following conclusions reflect a robust understanding of the study's themes:

707 The study area's surface sediments consist of ten types, including gravelly sand, sandy
708 gravel, silty gravel, sandy silt, silt, gravelly silt, sand, gravelly sandy silt, gravelly sand, and silty
709 gravelly sand. Among these, gravelly sand and gravelly sand are the predominant types.

710 During the transition from flood to ebb tide, the flow field outside the estuary is driven by
711 the deflection of water currents from Beili Bay and Changhua Port, shifting the flow direction
712 from northeast to southwest. During the transition from ebb to flood tide, the deflection is
713 primarily influenced by the circulation outside Changhua Port, shifting the flow direction from
714 southwest to northeast.

715 The main sedimentation areas within the study area's river channels include Xiantiacun,
716 Danchangcun, and Jiuxiancun. The first two experience sediment deposition near the river
717 mouth's sand spit, while the latter's sediment is primarily deposited near the river bifurcation.

718 Regardless of whether it is the dry season or the flood season, the residual currents in the
719 study area are directed towards Beilun Bay (SWS), implying that sediments in the lower reaches
720 of the Changhua River will be influenced by the residual currents and transported towards Beili
721 Bay. The sand spit at the river mouth, affected by the southward residual currents, will cause
722 sediments from the north to be transported towards the northeast and southwest of the sand spit,
723 leading to its elongation. There exists a counterclockwise residual current eddy beneath Topped
724 wall Angle, and it is timed with a clockwise residual current eddy above Junbi Jiao. The river's
725 discharge has little impact on Channel A, but it significantly affects Channels B and C.

726

删除[Yuxi Wu]: Model Validation and Effectiveness: The sediment transport model has been rigorously validated using both theoretical and empirical methods. The theoretical validation was conducted using the sediment transport rate method, while empirical validation involved comparing th ...

删除[Yuxi Wu]: Deposition Patterns: The study reveals the deposition patterns in the estuary and downstream river channel of the Changhua River, which are closely related to the interplay between hydrodynamic conditions and geological settings. Specifically, the estuary's deposition is primarily ...

727 **Data Availability**

728 This study utilized shoreline data obtained free from the Geophysical Data System (GEODAS) at
729 https://www.ngdc.noaa.gov/mgg/gdas/gx_announce.html; The wind field data are available from
730 European Centre for Medium-Range Weather Forecasts (ECMWF) at
731 <https://cds.climate.copernicus.eu/cdsapp#!/dataset/reanalysis-era5-single-levels?tab=form>; In this
732 study part topographic data was obtained from the ETOPO1 dataset, developed by NOAA, which
733 includes comprehensive bathymetric and topographic information. The dataset has a resolution
734 of 1 arc-minute and is widely used for various geophysical applications." [DOI:
735 10.7289/V5C8276M]; Topographic data measured by ADCP and hydrological station data that
736 support the findings of this study are available from Haikou Marine Geological Survey Center
737 but restrictions apply to the availability of these data, which were used under license for the
738 current study, and so are not publicly available. Data are however available from the authors
739 upon reasonable request and with permission of Haikou Marine Geological Survey Center.

740 **Author contribution**

741 **Yuxi Wu:** Writing – review & editing, Writing – original draft, Visualization, Validation, Software,
742 Resources, Methodology, Investigation, Formal analysis, Data curation, Conceptualization. **Enjin**
743 **Zhao:** Writing – review & editing, Writing – original draft, Supervision, Resources, Project
744 administration, Conceptualization. **Xiwen Li:** Investigation (data collection), Validation,
745 Supervision, Project administration. **Shiyong Zhang:** Investigation (data collection), Validation.

746 **Competing interests**

747 The contact author has declared that none of the authors has any competing interests.

748 **Acknowledgments**

749 Acknowledgment section of the article contain the following:

750 This work was supported by the National Natural Science Foundation of China (Grant Nos.
751 52371295, 52001286), the Guangdong Basic and Applied Basic Research Foundation (Grant Nos.
752 2022A1515240002), the Hubei Provincial Natural Science Foundation of China (Grant No.
753 2023AFB576) and the China Geological Survey Project (DD20220956).

754 The authors are grateful to Haikou Marine Geological Survey Center, China Geological Survey
755 for providing data and technical support. Technical assistance during the field measurement
756 campaign is duly acknowledged.

757 The authors are grateful to Copernicus Climate Change Service: ERA5 hourly data on single
758 levels from 1940 to present (2021-2023) was downloaded from the Copernicus Climate Change
759 Service (2024).

760 The authors are grateful to Hainan Geographic Information Public Service Platform: The map in
761 this paper is quoted from Map World • Hainan (<https://hainan.tianditu.gov.cn/>), a website
762 developed by Hainan Geographic Information Public Service Platform.

763

删除[Yuxi Wu]: **Funding**

The text ends with an acknowledgment section and statement that includes:

National Natural Science Foundation of China (Grant Nos. 52371295, 52001286),

Guangdong Basic and Applied Basic Research Foundation (Grant Nos. 2022A1515240002),

Hubei Provincial Natural Science Foundation of China (Grant No. 2023AFB576)

设置格式[Yuxi Wu]: 正文, 行距: 2 倍行距, 图案: 清除(白色)

764 **Appendix A. Supplementary data**

765 The following is the Supplementary material related to this article.

766 **Table A.1 List of main parameters of survey vessel**

<u>Parameter</u>	<u>Value</u>	<u>Instrument diagram</u>
<u>LOA</u>	<u>11 m</u>	
<u>Breadth</u>	<u>2.8 m</u>	
<u>Modeled Depth</u>	<u>1.2 m</u>	
<u>Design Draft</u>	<u>0.8 m</u>	
<u>Speed</u>	<u>6.0 kn</u>	
<u>Hull Material</u>	<u>Fiber-reinforced plastic (FRP)</u>	

767 **Table A.2 List of main parameters of ADCP**

<u>Main parameters</u>	<u>Value</u>	<u>Instrument diagram</u>
<u>Working frequency</u>	<u>600 kHz</u>	
<u>Velocity accuracy</u>	<u>±0.3% ± 3 mm/s</u>	
<u>Velocity resolution</u>	<u>1 mm/s</u>	
<u>Velocity range</u>	<u>±10 m/s</u>	
<u>Layer thickness</u>	<u>0.5 m ~ 4 m</u>	
<u>Number of plies</u>	<u>1 - 128</u>	
<u>Temperature sensor range</u>	<u>-10 °C ~ +85 °C</u>	
<u>Accuracy of temperature sensor</u>	<u>±0.5 °C</u>	

768

769

设置格式[Yuxi Wu]: 字体: (默认) Times New Roman, ...

设置格式[Yuxi Wu]: 制表位: 不在 3.43 字符, 无项目符 ...

设置格式[Yuxi Wu]: 字体: (默认) Times New Roman, ...

设置格式[Yuxi Wu]: 段落间距段前: 1 行

带格式表格[Yuxi Wu]

设置格式[Yuxi Wu]: 字体: 10 磅

设置格式[Yuxi Wu]: 与下段同页

设置格式[Yuxi Wu]: 字体: 10 磅

设置格式[Yuxi Wu]: 字体: (中文) Times New Roman, ...

带格式表格[Yuxi Wu]

设置格式[Yuxi Wu]: 字体: 10 磅

设置格式[Yuxi Wu]: 与下段同页

设置格式[Yuxi Wu]: 字体: 10 磅

设置格式[Yuxi Wu]: 字体: (中文) Times New Roman, ...

设置格式[Yuxi Wu]: 字体: 10 磅

设置格式[Yuxi Wu]: 与下段同页

设置格式[Yuxi Wu]: 字体: 10 磅

设置格式[Yuxi Wu]: 字体: (中文) Times New Roman, ...

设置格式[Yuxi Wu]: 字体: 10 磅

设置格式[Yuxi Wu]: 与下段同页

设置格式[Yuxi Wu]: 字体: 10 磅

设置格式[Yuxi Wu]: 字体: 10 磅

设置格式[Yuxi Wu]: 字体: (中文) Times New Roman, ...

设置格式[Yuxi Wu]: 字体: 10 磅

设置格式[Yuxi Wu]: 与下段同页

设置格式[Yuxi Wu]: 字体: 10 磅

设置格式[Yuxi Wu]: 字体: 10 磅

设置格式[Yuxi Wu]: 字体: 10 磅

770

Table A.3 List of main parameters of clam grab sampler

<u>Main parameters</u>	<u>Value</u>	<u>Instrument diagram</u>
<u>Operational depth</u>	<u>≤ 50 m</u>	
<u>Material</u>	<u>Stainless steel</u>	
<u>Sampling area</u>	<u>500 cm²</u>	
<u>Weight</u>	<u>9 kg</u>	
<u>Maximum sampling volume</u>	<u>3.5 L</u>	

771

Table A.4 List of main parameters of laser particle size analyzer

<u>Main parameters</u>	<u>Value</u>	<u>Instrument diagram</u>
<u>Measuring principle (dry)</u>	<u>0.1 μ to 2500 μ</u>	
<u>Measuring principle (wet)</u>	<u>0.04 μ to 2500 μ</u>	
<u>Dry dispersion</u>	<u>Venturi/free fall</u>	
<u>Repeatability</u>	<u>< 1%</u>	
<u>Precision</u>	<u>< 3%</u>	
<u>Weight</u>	<u>55 kg</u>	
<u>Volume</u>	<u>35 inches× 21 inches× 17 inches</u>	

772

773

References

775 Adnan, R.M., Liang, Z.M., El-Shafie, A., Zounemat-Kermani, M., Kisi, O.: Prediction of
 776 Suspended Sediment Load Using Data-Driven Models, *Water*, 11(10), 2060. doi:

设置格式[Yuxi Wu]: 制表位: 不在 3.43 字符, 无项目符号
或编号

777 10.3390/w11102060, 2019.

778 Addison - Atkinson, W., Chen, A.S., Memon, F.A., Anta, J., Naves, J., Cea, L.: Investigation of
779 uniform and graded sediment wash-off in an urban drainage system: Numerical model
780 validation from a rainfall simulator in an experimental facility, *Journal of Hydrology*, 629,
781 130561. doi: 10.1016/j.jhydrol.2023.130561, 2024.

782 Auguste, C., Nader, J.R., Marsh, P., Cossu, R., Penesis, I.: Variability of sediment processes
783 around a tidal farm in a theoretical channel, *Renewable Energy*, 171, 606-620. doi:
784 10.1016/j.renene.2021.02.147, 2021.

785 Bai, J., Fang, H. W., He, G.J., Xie, C. B., Gao, H.: Numerical simulation of erosion and transport
786 of fine sediments by large eddy simulation. *Chinese Journal of Theoretical and Applied*
787 *Mechanics*, 49(1), 65-74. doi: 10.6052/0459-1879-16-235, 2017.

788 Bakhtyar, R., Barry, D.A., Li, L. Jeng, D. S.: Yeganeh-Bakhtiary, A.: Modeling sediment
789 transport in the swash zone: A review, *Ocean Engineering*, 36, (9-10), 767-783, doi:
790 10.1016/j.oceaneng.2009.03.003, 2009.

791 Blumberg, A. F., Mellor, G. L.: A description of a three-dimensional coastal ocean circulation
792 model. *Coastal and Estuarine Sciences*, 4, 1-16. doi: 10.1029/CO004p0001, 1987.

793 Brenna, A., Marchi, L., Borga, M., Zaramella, M., Surian, N. : What drives major channel
794 widening in mountain rivers during floods? The role of debris floods during a
795 high-magnitude event, *Geomorphology*, 430, 108650.
796 doi: 10.1016/j.geomorph.2023.108650, 2023.

797 Bui, L. H. N., Bui, L. T.: Modelling bank erosion dependence on natural and anthropogenic
798 factors — case study of Ganh Hao estuary, Bac Lieu - Ca Mau, Vietnam, *Environmental*
799 *Technology & Innovation*, 19, 100975. doi: 10.1016/j.eti.2020.100975, 2020.

800 Bijker, E. W.: Some considerations about scales for coastal models with movable bed, Delft
801 Hydraulics Laboratory publication, 50. doi:
802 <https://repository.tudelft.nl/record/uuid:cdf2f061-3fe6-4361-a0e7-636fc69c9eca>,1967.

803 Chen, W.Q., Werf, J.J., Hulscher, S.J.M.H.: Practical modelling of sand transport and beach
804 profile evolution in the swash zone, *Coastal Engineering*, 191, 104514. doi:
805 10.1016/j.coastaleng.2024.104514, 2024.

806 [Chen, C., Liu, H., Beardsley, R. C.: An unstructured grid, finite-volume, three-dimensional,](#)
807 [primitive equations ocean model: application to coastal ocean and estuaries. *Journal of*](#)
808 [*atmospheric and oceanic technology*, 20\(1\): 159-186. doi:](#)
809 [10.1175/1520-0426\(2003\)020<0159:AUGFVT>2.0.CO;2, 2003.](#)

设置格式[Yuxi Wu]: 字体: 倾斜

810 [Chen, C., Xue, P., Ding, P., Beardsley, R. C., Xu, Q., Mao, X., Gao, G., Qi, J., Li, C., Lin, H.,](#)
811 [Cowles, G., Shi, M.: Physical mechanisms for the offshore detachment of the Changjiang](#)
812 [Diluted Water in the East China Sea. *Journal of Geophysical Research: Oceans*, 113\(C2\).](#)
813 [doi: 10.1029/2006JC003994, 2008.](#)

设置格式[Yuxi Wu]: 字体: 倾斜

814 [Chen, T., Zhang, Q., Wu, Y., Ji, C., Yang, J., Liu, G.: Development of a wave-current model](#)
815 [through coupling of FVCOM and SWAN, *Ocean Engineering*, 164, 443-454. doi:](#)
816 [10.1016/j.oceaneng.2018.06.062, 2018.](#)

设置格式[Yuxi Wu]: 字体: 倾斜

817 Claude, N., Rodrigues, S., Bustillo, V., Br      , J.G., Macaire, J.J., Jug  , P.: Estimating bedload
818 transport in a large sand–gravel bed river from direct sampling, dune tracking and empirical
819 formulas, *Geomorphology*, 179, 40-57. doi: 10.1016/j.geomorph.2012.07.030, 2012.

820 Clift, P.D., Plumb, R.A.: The Asian Monsoon: Causes, History and Effects. *Cambridge*
821 *University Press*, 37(3), 92-93. doi: 10.1017/CBO9780511535833, 2008.

822 Constant, M., Alary, C., Weiss, L., Constant, A., Billon, G.: Trapped microplastics within vertical
823 redeposited sediment: Experimental study simulating lake and channeled river systems
824 during resuspension events, *Environmental Pollution*, 322, 121212. doi:
825 10.1016/j.envpol.2023.121212, 2023.

826 Doroudi, S., Sharafati, A.: A newly developed multi-objective evolutionary paradigm for
827 predicting suspended sediment load, *Journal of Hydrology*, 634, 131090. doi:
828 10.1016/j.jhydrol.2024.131090, 2024.

829 Ding, Q.L.: Wave characteristics and calculation of Beibu Gulf. *Marine Forecasts*, 7 (2): 46-52.
830 doi: 10.11737/j.issn.1003-0239.1990.02.007, 1990.

831 Fang, X., Zou, J., Wu, Y., Zhang, Y., Zhao, Y., Zhang, H.: Evaluation of the sustainable
832 development of an island “Blue Economy”: a case study of Hainan, China. *Sustainable*
833 *Cities and Society*, 66, 102662. doi: 10.1016/j.scs.2020.102662, 2021.

834 Feng, H.L., Liu, M., Xu, M.Y., Zhang, M.X., Mo, L., Chen, T., Tan, X.Y., Liu, Z.Y.: Study on the
835 integrated protection strategy of water environment protection: The case of Hainan Province
836 of China. *Environmental Technology & Innovation*, 24, 101990. doi:
837 10.1016/j.eti.2021.101990, 2021.

838 Gao, J.: Study on sediment transport model in Changhua River Estuary of Hainan Province based

839 on remote sensing analysis. *China University of Geosciences (Beijing)*. doi: CNKI: CDMD:
840 2.1014.101980080086, 2014.

841 Gessler, D., Hall, B., Spasojevic, M., Holly, F. M., Pourtaheri, H., Raphael, N. X.: Application of
842 3D mobile bed, hydrodynamics model. *Journal of Hydraulic Engineering*, 125(7), 737-749.
843 doi: 10.1061/(ASCE)0733-9429(1999)125:7(737), 1999.

844 Han, X.J., Kuang, C.P., Gong, L.X., Li, W.B.: Sediment transport and seabed evolution under
845 artificial headland and beach nourishment engineering. *Oceanologia et Limnologia Sinica*,
846 53(4), 917-932. doi: 10.11693/hyhz20211200345, 2022.

847 Holly, F. M., Rahuel, J. L.: New numerical/physical framework for mobile-bed modeling. Part 1:
848 Numerical and physical principles. *Journal of Hydraulic Research*, 28(4), 401-416. doi:
849 10.1080/00221689009499057, 1990.

850 Hu, X.Z.: Mathematical Simulation Study of Sediment in Intake and Outfall of Dongfang (East)
851 Power Plant in Hainan at North Bay. *Pearl River*, 030 (006): 18-23. doi:
852 10.3969/j.ISSN.1001-9235.2009.06.006, 2009.

853 Huang, H., Chen, C., Blanton, J. O., Andrade, F. A.: A numerical study of tidal asymmetry in
854 Okatee Creek, South Carolina. *Estuarine, Coastal and Shelf Science*, 78(1): 190-202. doi:
855 10.1016/j.ecss.2007.11.027, 2008.

856 Jia, Y., Wang, S. S.: Numerical model for channel flow and morphological change
857 studies. *Journal of Hydraulic Engineering*, 125(9), 924-933. doi:
858 10.1061/(ASCE)0733-9429(1999)125:9(924), 1999.

859 Jin, J., Ou-Yang, Z.Y., Lin, S.K., Wang, X.K.: A study on ecosystem deterioration and protection
860 counter-measure of Hainan Island coast. *Ocean Development and Management*, 2008(1),

设置格式[Yuxi Wu]: 字体: 倾斜

- 861 103-108. doi: 10.20016/j.cnki.hykyfjgl.2008.01.022, 2008.
- 862 Jiang, L., Xia, M.: Dynamics of the Chesapeake Bay outflow plume: Realistic plume simulation
863 and its seasonal and interannual variability. *Journal of Geophysical Research: Oceans*,
864 121(2): 1424-1445. doi: 10.1002/2015JC011191, 2016. 设置格式[Yuxi Wu]: 字体: 倾斜
- 865 Ji, C., Zhang, Q., Ma, D., Wu, Y., Jiang, Q.: Nearshore coupled wave-current model based on
866 new three-dimensional radiation stress formulation. *Journal of Zhejiang University*
867 (*Engineering Science*), 56(1), 128-136. doi: 10.3785/j.issn.1008-973X.2022.01.014. 设置格式[Yuxi Wu]: 字体: 倾斜
- 868 Leary, K.C.P., Buscombe, D.: Estimating sand bed load in rivers by tracking dunes: a comparison
869 of methods based on bed elevation time series, *Earth Surface Dynamics*, 8, 161-172.
870 doi: 10.5194/ESURF-8-161-2020, 2020.
- 871 Lee, H. Y., Hsieh, H. M., Yang, J. C., Yang, C. T.: Quasi-two-dimensional simulation of scour
872 and deposition in alluvial channels. *Journal of Hydraulic Engineering*, 123(7), 600-609. doi:
873 10.1061/(ASCE)0733-9429(1997)123:7(600), 1997.
- 874 Liu, J., Bai, Y.C.: The interactions between wave and cohesive sediment. *Mechanics in*
875 *Engineering*, 36(3), 253-260. doi: 10.6052/1000-0879-13-204, 2014.
- 876 Lai, W., Pan, J., Devlin, A. T.: Impact of tides and winds on estuarine circulation in the Pearl
877 River Estuary. *Continental Shelf Research*, 168, 68-82. doi: 10.1016/j.csr.2018.09.004,
878 2018. 设置格式[Yuxi Wu]: 字体: 倾斜
- 879 Longuet-Higgins, M.S.: On the transport of mass by time-varying ocean currents. *Deep Sea*
880 *Research and Oceanographic Abstracts*, 16(5), 431-447. doi:
881 10.1016/0011-7471(69)90031-X, 1969. 设置格式[Yuxi Wu]: 字体: 倾斜

882 [Li, C., O'Donnell, J.: Tidally driven residual circulation in shallow estuaries with lateral depth](#)
883 [variation. *Journal of Geophysical Research*, 102\(C13\), 27915–27929,](#)
884 [doi:10.1029/97JC02330. 1997.](#)

设置格式[Yuxi Wu]: 字体: 倾斜

885 Mao, L.M., Zhang, Y.L., Bi, H.: Modern pollen deposits in coastal mangrove swamps from
886 northern Hainan Island, China. *Journal of Coastal Research*, 22 (6), 1423-1436. doi:
887 10.2112/05-0516.1, 2006.

888 Michel, G., Le Bot, S., Deloffre, J., Legrain, M., Levailant, R., Simon, M., Tessier, B., Lesourd,
889 S.: In-situ characterisation of fluvial dune morphology and dynamics under limited
890 sediment supply conditions, Seine River, France, *Geomorphology*, 439, 108855. doi:
891 10.1016/j.geomorph.2023.108855, 2023.

892 Miluch, J., Maciąg, L., Osadczuk, A., Harff, J., Jiang, T., Chen, H.J., Krzysztof Borówka, R.,
893 Kevin-McCartney.: Multivariate geostatistical modeling of seismic data: Case study of the
894 Late Pleistocene paleodelta architecture (SW off-shore Hainan Island, south China sea),
895 *Marine and Petroleum Geology*, 136, 105467. doi: 10.1016/j.marpetgeo.2021.105467,
896 2022.

897 Ministry of Water Resources of the People's Republic of China: Code for design of river
898 regulation. *Ministry of Housing and Urban-Rural Development of the People's Republic of*
899 *China State Administration of Quality Supervision*, GB 50707-2011, 2011.

900 Mohd-Salleh, S.H., Ahmad, A., Wan-Mohtar, W.H.M., Lim, C.H., Abdul-Maulud, K.N.: Effect of
901 projected sea level rise on the hydrodynamic and suspended sediment concentration profile
902 of tropical estuary, *Regional Studies in Marine Science*, 24, 225-236.
903 doi:10.1016/j.rsma.2018.08.004, 2018.

- 904 [Maddock, L., Pingree, R.D.: Numerical simulation of the Portland tidal eddies. *Estuarine and*](#)
905 [*Coastal Marine Science*, 6\(4\), 353-363. doi: 10.1016/0302-3524\(78\)90127-5, 1978.](#) 设置格式[Yuxi Wu]: 字体: 倾斜
- 906 Nash, J.E., Sutcliffe, J.V.: River flow forecasting through conceptual models part I — A
907 discussion of principles, *Journal of Hydrology*, 10 (3), 282-290. doi:
908 10.1016/0022-1694(70)90255-6, 1970.
- 909 Niu, J., Xie, J., Lin, S., Lin, P., Gao, F., Zhang, J., Cai, S.: Importance of bed
910 liquefaction-induced erosion during the winter wind storm in the Yellow River Delta, China,
911 *Journal of Geophysical Research: Oceans*, 128(10), e2022JC019256. doi:
912 10.1029/2022JC019256, 2023.
- 913 Nowacki, D.J., Grossman, E.E.: Sediment transport in a restored, river-influenced Pacific
914 Northwest estuary. *Estuarine, Coastal and Shelf Science*, 242, 106869. doi:
915 10.1016/j.ecss.2020.106869, 2020.
- 916 Orseau, S., Huybrechts, N., Tassi, P., Pham Van Bang, D., Klein, F.: Two-dimensional modeling
917 of fine sediment transport with mixed sediment and consolidation: Application to the
918 Gironde Estuary. *International Journal of Sediment Research*, 36(6), 736-746. doi:
919 10.1016/j.ijsrc.2019.12.005, 2021.
- 920 Papanicolaou, A., Bdour, A., Wicklein, E.: One-dimensional hydrodynamic/sediment transport
921 model applicable to steep mountain streams. *Journal of Hydraulic Research*, 42(4),
922 357-375. doi: 10.1080/00221686.2004.9728402, 2004.
- 923 [Pingree, R.D., Maddock, L.: Tidal residuals in the English Channel. *Journal of the Marine*](#)
924 [*Biological Association of the United Kingdom*, 57, 339-354. doi:](#) 设置格式[Yuxi Wu]: 字体: 倾斜
925 [10.1017/S0025315400021792, 1977.](#)

926 Pradhan, U.K., Mishra, P., Mohanty, P.K., Panda, U.S., Ramanamurthy, M.V.: Modeling of tidal
927 circulation and sediment transport near tropical estuary, east coast of India. *Regional Studies*
928 *in Marine Science*, 37, 101351. doi: 10.1016/j.rsma.2020.101351, 2020.

929 Qi, Y.L., Yu, Q., Gao, S., Li, Z.Q., Fang, X., Guo, Y.H.: Morphological evolution of river mouth
930 spits: Wave effects and self-organization patterns. *Estuarine, Coastal and Shelf Science*, 262,
931 107567. doi: 10.1016/j.ecss.2021.107567, 2021.

932 Robinson, I. S.: Chapter 7 Tidally Induced Residual Flows. *Elsevier Oceanography*, 35: 321-356.
933 doi: 10.1016/S0422-9894(08)70505-1, 1983.

设置格式[Yuxi Wu]: 字体: 倾斜

934 Sarwar, S., Borthwick, A.G.L.: Estimate of uncertain cohesive suspended sediment deposition
935 rate from uncertain floc size in Meghna estuary, Bangladesh. *Estuarine, Coastal and Shelf*
936 *Science*, 281, 108183. doi: 10.1016/j.ecss.2022.108183, 2023.

937 Spasojevic, M., Holly, F.M.: 2-D bed evolution in natural watercourses—new simulation
938 approach. *Journal of Waterway, Port, Coastal, and Ocean Engineering*, 116(4), 425-443.
939 doi: 10.1061/(ASCE)0733-950X(1990)116:4(425), 1990.

940 Smith, P.C.: The Mean and Seasonal Circulation off Southwest Nova Scotia, *Journal of*
941 *Physical Oceanography*, 13, 1034-1054. doi: 10.1175/1520-0485(1983)013<1034:TMA
942 *SCO>2.0.CO;2*, 1983.

设置格式[Yuxi Wu]: 允许西文在单词中间换行

设置格式[Yuxi Wu]: 字体: 倾斜

943 Terêncio, D.P.S., Pacheco, F.A.L., Valle-Junior, R.F., Melo-Silva, M.M.A.P., Pissarra, T.C.T.,
944 Melo, M.C., Valera, C.A., Fernandes, L.F.S.: The Igarapé Weir decelerated transport of
945 contaminated sediment in the Paraopeba River after the failure of the B1 tailings dam
946 (Brumadinho). *International Journal of Sediment Research*, 38(5), 673-697. doi:
947 10.1016/j.ijsrc.2023.06.004, 2023.

948 Thomas, W.A., Prashum, A.I.: Mathematical model of scour and deposition. *Journal of the*
949 *Hydraulics Division*, 103(8), 851-863. doi: 10.1061/JYCEAJ.0004805, 1977.

950 Uncles, R.J., Jordan, M.B.: A one-dimensional representation of residual currents in the Severn
951 Estuary and associated observations. *Estuarine and Coastal Marine Science*, 10(1), 39-60.
952 doi: 10.1016/S0302-3524(80)80048-X, 1980.

设置格式[Yuxi Wu]: 字体: 倾斜

953 Van-Rijn, L.C.: Sediment Transport, Part I : Bed load transport. *Journal of Hydraulic*
954 *Engineering*, 110(10),1431-1455. doi: 10.1061/(ASCE)0733-9429(1984)110:10(1431),
955 1984.

956 Vázquez-Tarrío, D., Ruiz-Villanueva, V., Garrote, J., Benito, G., Calle, M., Lucía, A.,
957 Díez-Herrero, A.: Effects of sediment transport on flood hazards: Lessons learned and
958 remaining challenges, *Geomorphology*, 446, 108976. doi: 10.1016/j.geomorph.2023.108976,
959 2024.

960 Vinzon, S.B., Gallo, M.N., Gabioux, M., Fonseca, D.L., Achete, F.M., Ghisolfi, R.D., Mill, G.N.,
961 Fonseca, S.A.R., Silva-Quaresma, V., Oliveira, K.S.S., Brigagão, G., Machado, L.G.: The
962 role of waves in the resuspension and transport of fine sediment and mine tailings from the
963 Fundão Dam failure, Doce River, Brazil, *International Journal of Sediment Research*, 39(1),
964 44-60. doi: 10.1016/j.ijsrc.2023.09.004, 2023.

965 Wang, D., Pei, L., Zhang, L., Li, X., Chen, Z., Zhou, Y.: Water resource utilization characteristics
966 and driving factors in the Hainan Island. *Journal of Groundwater Science and Engineering*,
967 11(2), 191-206. doi: 10.26599/JGSE.2023.9280017, 2023.

968 Wang, X.M., Qu, H.B., Xiong, Y.K., Lu, L., Hu, K.: Grain-size characteristics and transport trend
969 of bottom sediments at the estuary of Changhua River in Hainan. *Geoscience*, 36 (1), 88-95.

970 doi: 10.19657/j.geoscience.1000-8527.2021.1720001106, 2022.

971 Wang, Y.: Environmental characteristics of Hainan Island coast. *Marine Geology letters*, 18(3),
972 1-9. doi: CNKI:SUN:HYDT.0.2002-03-000, 2002.

973 Wang, X.H.: Analysis of wave characteristics in the offshore area of Dongfang City. *Marine*
974 *Sciences*, 47(2), 31-46. doi:10.11759/hyqx20220919001, 2023.

975 Wu, J.Q., Xiao, M., Yang, J.T., Xiao, X.B., Tang, W.H.: Study on distribution characteristics of
976 soil erosion in the lower reaches of Changhua River in Hainan. *Technology of Soil and*
977 *Water Conservation*, 2012(3), 12-15. doi: 10.3969/j.issn.1673-5366.2012.03.04, 2012.

978 Wu, W., Rodi, W., Wenka, T.: 3D numerical modeling of flow and sediment transport in open
979 channels. *Journal of Hydraulic Engineering*, 126(1), 4-15. doi:
980 10.1061/(ASCE)0733-9429(2000)126:1(4), 2000.

981 Yang, Z.H., Jia, J.J., Wang, X.K., Gao, J.H.: Characteristics and variations of water and sediment
982 fluxes into the sea of the top three rivers of Hainan in recent 50 years. *Marine Science*
983 *Bulletin*, 32 (1), 92-99. doi: 10.11840/j.issn.1001-6392.2013.01.014, 2013.

984 Zeng, Z.X., Zeng, X.Z.: *Physicogeography of Hainan Island*. Science Press, Beijing, 1989.

985 Zhang, L.M., Wei, Z.Y., Cao, Q.M., Sang, A.Y., Wang, H., Qi, Z.P.: Characteristics and
986 influencing factors of sediment concentration in the lower reaches of three major rivers in
987 Hainan Province in recent 40 years. *Ecology and Environmental Sciences*, 15(4), 765–769.
988 doi: 10.3969/j.issn.1674-5906.2006.04.022, 2006.

989 Zhang, P., Ruan, H.M., Dai, P.D., Zhao, L.R., Zhang, J.B.: Spatiotemporal river flux and
990 composition of nutrients affecting adjacent coastal water quality in Hainan Island. *Journal*
991 *of Hydrology*, 591, 125293. doi: 10.1016/j.jhydrol.2020.125293, 2020.

992 Zhang, W.Y., Xiong, P., Meng, Q.C., Dudzinska-Nowak, J., Chen, H., Zhang, H., Zhou, F.,
993 Miluch, J., Harff, J.: Morphogenesis of a late Pleistocene delta off the south-western Hainan
994 Island unraveled by numerical modeling, *Journal of Asian Earth Sciences*. 195, 104351. doi:
995 10.1016/j.jseaes.2020.104351, 2020.

996 Zhao, L., Cai, G.Q., Zhong, H.X., Li, B., Zou, L.Q., Li, S., Han, Y.F.: Grain-size characteristics
997 and sedimentary environment of surface sediments in the shallow sea in the southeast of
998 Hainan Island. *Marine Geology & Quaternary Geology*, 41(2), 64-74. doi:
999 10.6562/j.cnki.5566-1992585866, 2021.

1000 Zhu, L.R., Liu Y.H., Ye, C.Q.: Runoff change and influencing factors of Changhua River in arid
1001 area of Hainan Island. *Ecological Science*, 39 (1), 183-189. doi: CNKI: Sun:
1002 STKX.0.2020-01-023, 2020.

1003 Zimmerman, J.: Dynamics, diffusion and geomorphological significance of tidal residual eddies.

1004 *Nature*, 290, 549–555. doi: 10.1038/290549a0, 1981.

设置格式[Yuxi Wu]: 字体: 倾斜